

# **3D Architecture Electrodes for Energy Storage Applications**

**by  
Seong hyeon Park**

B.S., University of Texas at El Paso, 2015

Thesis Submitted in Partial Fulfillment of the  
Requirements for the Degree of  
Master of Applied Science

in the  
School of Mechatronic Systems Engineering  
Faculty of Applied Science

© Seong hyeon Park  
SIMON FRASER UNIVERSITY  
Fall 2018

Copyright in this work rests with the author. Please ensure that any reproduction or re-use is done in accordance with the relevant national copyright legislation.

# Approval

**Name:** Seong hyeon Park  
**Degree:** Master of Applied Science  
**Title:** *3D Architecture Electrodes for Energy Storage Applications*  
**Examining Committee:** **Chair: Jiacheng (Jason) Wang**  
Assistant Professor

**Woo Soo Kim**  
Senior Supervisor  
Associate Professor

**Kevin Oldknow**  
Supervisor  
Senior Lecturer & Associate Dean

**Ash M. Parameswaran**  
Internal Examiner  
Professor  
School of Engineering Science

**Date Defended/Approved:** December 10, 2018

## **Abstract**

Micro-scale energy storage devices have been developed for the demand of required energy autonomy of the portable and small-scale electronics. One main drawback in realization of micro-scale energy storage devices is limited areal capacitance due to low material loading per unit area on the substrate. 3-D electrodes with high aspect ratio could be promising strategy to overcome this, resulting in higher device performance. Specially, 3D printing technology offers numerous advantages to generate 3D electrodes for energy storage devices, which includes time-saving, cost-effective manufacturing, and realization of tailorable complex electrode designs. In this thesis, novel hierarchical 3D designs were printed by photo-curable 3D printing. Photo-curable resins with conductive fillers were optimized for conductive 3D electrode formation. Finally, energy storage devices with the hierarchical 3D electrodes have been demonstrated for the application of micro-supercapacitors (MSCs). The fabricated 3D hierarchical electrodes demonstrated low electrical resistance to be used as feasible MSCs electrodes. Energy storage from redox reactions was demonstrated in 3D architecture electrodes designed with mechanically durable 3D octet trusses.

**Keywords:** 3D printing; Micro supercapacitor; 3D architecture

*I would like to dedicate my thesis to my beloved family*

## **Acknowledgements**

I would like to express my sincere gratitude to my senior supervisor, Dr. Woo Soo Kim, for the continuous support of Master's degree study and research. His patient guidance and encouragement helped me in all the time of the research. I have learned the methodology to carry out the research and to present the research works as concise as possible and clearly.

I also would like to thank my thesis committee members, Dr. Kevin Oldknow for being my supervisor, Dr. Ash M. Parameswaran for being my Internal examiner and Dr. Jiacheng (Jason) Wang for being committee examine Chair who were willing to review my thesis.

It has been a great two years with my lab mates; Manpreet, Taeil, Yue, Chao and Xin. They were always kind and positive. We had an amazing outdoor BBQ and dinner at home.

I want to thank Cody and Leanne, who are my roommates for 2 years during my master program. Whenever I had hard time on living in Vancouver or the research work, with them, my home was the best place to find peace. They tried to show me all about Vancouver. I really enjoyed the life in Canada with them.

I truly thank my family who were always providing me any supports.

# Table of Contents

Approval.....	ii
Abstract.....	iii
Dedication.....	iv
Acknowledgements.....	v
Table of Contents.....	vi
List of Tables .....	viii
List of Figures .....	ix
List of Acronyms .....	xi
<b>Chapter 1. Introduction.....</b>	<b>1</b>
1.1. Motivation.....	1
1.2. Objective .....	3
1.3. Contribution.....	3
1.4. Thesis Organization .....	4
<b>Chapter 2. Literature review .....</b>	<b>5</b>
2.1. Principle of Supercapacitor.....	5
2.1.1. Electric double layer capacitor & Pseudo capacitor .....	5
2.2. Development of Micro-supercapacitor .....	6
2.2.1. Design of Electrode .....	6
2.2.2. 2D planar Micro-supercapacitor.....	8
2.2.3. Recent researches on 3D printed Micro-supercapacitor .....	11
2.2.3.1. Extrusion printed 3D Micro-supercapacitor.....	11
2.2.3.2. FDM / Electro spun printed 3D Micro-supercapacitor.....	14
2.2.3.3. Binder Jet Printed, Laser Processed 3D Micro-supercapacitor .....	16
<b>Chapter 3. Design and Optimization of photo-curable conductive resin .....</b>	<b>18</b>
3.1. Objective and Plan .....	18
3.2. 3D printing process .....	18
3.3. Composition of photo-curable resin .....	20
3.3.1. Monomer.....	20
3.3.2. Oligomer.....	21
3.3.3. Photo-initiator .....	22
3.3.4. Light induced polymerization .....	23
3.3.5. Photo-absorber.....	23
3.4. Printing quality on different ratio of the resin composition .....	25
3.5. Mechanical testing.....	27
3.6. Design of photo-curable conductive resin.....	28
3.6.1. Viscosity optimizaiton .....	29

3.6.2. Light absorbing sensitivity .....	30
<b>Chapter 4. Design of 3D Electrode.....</b>	<b>32</b>
4.1. Interdigitated electrode embeded with truss structrue.....	32
4.2. Pyrolysis of designed structrue.....	36
4.2.1. Experimental process .....	36
4.2.2. Charaterizaiton of pyrozed electrodes .....	37
4.2.2.1. Electrical resistance .....	37
4.2.2.2. Morphology & Composition analysis.....	38
<b>Chapter 5. 3D printed micro-supercapacitor.....</b>	<b>43</b>
5.1. Fabrication process .....	43
5.2. Performance evaluaiton of micro-supercapacitor.....	44
5.2.1. Cyclic Voltammetry .....	44
5.2.2. Galvanostatic charge/discardge .....	46
<b>Chapter 6. Conclusion and Future Work .....</b>	<b>47</b>
6.1. Conclusion .....	47
6.2. Future Works.....	48
<b>References .....</b>	<b>49</b>
<b>Appendix A. Resin cartridge of DLP printer.....</b>	<b>60</b>
<b>Appendix B. Resolution test .....</b>	<b>60</b>
<b>Appendix C. Silver nanowire synthesis.....</b>	<b>61</b>
<b>Appendix D. Printed samples on the platform .....</b>	<b>62</b>

## List of Table

Table 3.1.	Photographs of DLP printed octet structures with different parameters ..	26
Table 4.1.	Surface area analysis of unit cell of electrodes (Solid vs Octet-thick vs Octet-thin vs Double gyroid).....	33



## List of Figures

Figure 1.1.	Ragone plot for the various electrochemical energy conversion systems .	3
Figure 2.1.	Schematic of charge storage via the process of either (a) electrochemical double-layer capacitance or (b) pseudocapacitance [19].....	6
Figure 2.2.	Design of 2D to 3D electrode: (a) Thick film, (b) Nanostructured material, (c) nanostructured material + additive, (d) Graphene sheet with active material, (e) 3D monolithic electrode, (f) 3D monolithic current collector with active material .....	8
Figure 2.3.	MSCs with Two Dimensional Electrodes by (a) laser scribing, (b) laser sintering and (c) ink-jet printing methods.....	10
Figure 2.4.	Directly Written MSCs: Extrusion printing with (a) reduced graphene oxide, (b) CNT, (c) graphene/PANI, (d) V2O5 + GO, G-VNQDs + GO, LiCl with PVA. (e) Aerosol jet printing (AJP) with Ag nanoparticle .....	13
Figure 2.5.	FDM, Electro spun printed 3D MSCs: (a) FDM printing with graphene and PLA, electro spinning printed (b) 3D structure (c) 3D electrode .....	15
Figure 2.6.	Binder Jet Printed, Laser Processed 3D MSCs: (a) BIJ with graphene, (b) SLM with Ti6Al4V powders .....	17
Figure 3.1.	Schematic of DLP printing system .....	19
Figure 3.2.	Photograph of DLP printer, Projet 1200 from 3D systems .....	19
Figure 3.3.	Chemical structure of methacrylic acid.....	20
Figure 3.4.	UV-VIS spectra of MA.....	20
Figure 3.5.	Chemical structure of UTA .....	21
Figure 3.6.	Chemical structure of Irgacure 819 before and after fragmentation .....	22
Figure 3.7.	UV-VIS spectra of Irgacure (3wt% in MA) .....	22
Figure 3.8.	Chemical structure of Sudan I .....	23
Figure 3.9.	UV-VIS spectra of Sudan I (solid line).....	24
Figure 3.10.	Photograph of octet structure showing 500µm strut width .....	26
Figure 3.11.	Schematics of resin flow during DLP printing .....	27
Figure 3.12.	Stress versus strain graph under the compress test.....	28
Figure 3.13.	Photographs of DLP printed octet with/without AgNWs.....	31
Figure 4.1.	3D model of octet structure 4x4x4 (total 64-unit cells).....	33
Figure 4.2.	(A): 3D modeling of IDE-double gyroid with different aspect ratio (3 mm, 6 mm, and 12mm from left), (b): IDE-double gyroid as printed, (C) IDE-double gyroid after pyrolysis at 430 °C .....	34
Figure 4.3.	Comparison of different structures before and after pyrolysis.....	34
Figure 4.4.	(A–C) 3D model images of interdigitated electrodes (IDEs). (A): IDE-solid	

	with a different aspect ratio (3 mm, 6 mm, and 12 mm from left), (B): IDE-octet with thick (480 $\mu\text{m}$ ) strut size, (C): IDE-octet with thin (300 $\mu\text{m}$ ) strut size. (Inset: a unit cell of the octet, scale bar: 500 $\mu\text{m}$ )....	35
Figure 4.5.	Photographs of 3D printed IDE based on 3D modeling as printed (A, B, C), after pyrolysis (D, E, F). (Inset: digital microscope image) .....	36
Figure 4.6.	Contact points for electrical resistance measurement .....	37
Figure 4.7.	Plot of the resistances with respect to different pyrolysis temperature....	38
Figure 4.8.	Optical microscopy images with different magnification: IDE as printed in (A) and (B); IDE after pyrolysis in (C), and (D) .....	39
Figure 4.9.	Scanning electron microscope images of 3D printed IDE. (A–C) As printed. (D) EDS spectra of IDE as printed in the selected yellow area of (B) .....	40
Figure 4.10.	Scanning electron microscope images of 3D printed IDE (A–C) After pyrolysis. (D) EDS spectra of and IDE after pyrolysis in the selected yellow area of (B).....	41
Figure 4.11.	EDS spectra in char (A, B) and in silver (C, D).....	42
Figure 5.1.	Schematics of fabrication process of MSCs (Upper) Photographs of fabrication process (Lower), scale bar:10 mm .....	43
Figure 5.2.	Cyclic voltammetry curve; black is octet-thin and red is octet- thick .....	44
Figure 5.3.	Galvanostatic charge/discharge curve of IDE-Thin at 0.2 mA .....	46

## List of Acronyms

AgNW	Silver Nanowire
AJP	Aerosol Printing
BIJ	Binder Ink Jetting
CV	Cyclic voltammetry
DIW	Direct Ink Writing
DLP	Digital Light Processing
EDLC	Electric Double Layer Capacitor
EP	Extrusion Printing
FDM	Fused Deposition Modeling
GCD	Galvanostatic Charge/Discharge
IDC	Interdigitated Capacitor
IDE	Interdigitated Electrode
IPA	Isopropyl Alcohol
MA	Methacrylic Acid
MSC	Micro-supercapacitor
PCCR	Photo Curable Conductive Resin
PCR	Photo Curable Resin
PVA	Polyvinyl alcohol
SLM	Selective Laser Melting
UTA	Urethane tri acrylate

# Chapter 1

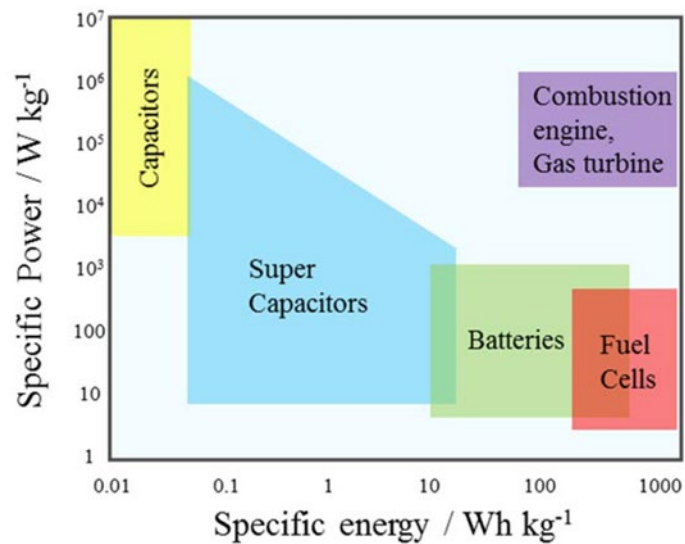
## Introduction

### 1.1. Motivation

Miniature electronic storage devices have been rapidly developed for the demand of required energy autonomy of the compact devices. As a candidate of energy/power sources, micro-supercapacitors (MSCs) have been selected because of high-power density, high rate capability, long charge/discharge cycles, and fast charge/discharge rates [2–4]. However, the limited capacitance of MSCs, which lead to low energy density, has restricted practical use despite of novel advantage of MSCs. For example, the energy density of supercapacitors has been reported in the range of 0.1 ~ 10 Wh/kg, while lithium-ion battery shows the energy density as 10 ~ 800 Wh/kg as shown in Figure 1 [1]. Specially, conventional 2D planar MSCs have shown limited areal capacitance due to low-volume loading of active materials per unit area. To enhance electrochemical performance while keeping a low MSCs footprint, more active materials need to be loaded per unit area of electrodes [5]. Therefore, 3D electrodes having a high aspect ratio with porous architecture have been adapted to achieve higher electrochemical performance. Several fabrication technologies have been introduced to develop 3D electrodes such as graphene aerogel [6], MEMS [7] (and C-CMEMS [8]), and templated synthesis (self-assembly method) [9]. However, these technologies have disadvantages such as high cost, complex fabrication, time-consuming, and use of toxic materials for the etching process [7] or removal of a template [9] after self-assembly.

As a novel fabrication method, 3D printing has been employed to fabricate 3D electrodes [10–13] to overcome those disadvantages. The interdigitated micro-battery by direct ink writing (DIW), where for the active materials,  $\text{Li}_4\text{Ti}_5\text{O}_{12}$  (LTO) and  $\text{LiFePO}_4$  (LFP), were reported as anode and cathode materials, respectively [10]. Also, the graphene oxide based interdigitated electrode by DIW was reported [11]. 3D interdigitated Ti6Al4V electrodes were introduced with selective laser melting (SLM) [12]. Recently, the graphene-based polylactic acid filament (graphene/PLA) electrode by fused deposition modeling (FDM) printing was also reported [13]. Recently, 3D printing for MSCs relatively offers not only facile, scalable, and fast fabrication but

also the freedom of designing a complex structure with a high aspect ratio for 3D electrodes. However, among other 3D printing methods, digital light processing (DLP) printing has not been explored much for the development of 3D electrodes, which have capability for higher resolution and complex designs. It is demonstrated that highly complex 3D architectures with micro- to mesoscales can be fabricated by DLP printing [14]. Moreover, it is suitable to generate porous or hollow structures because DLP printing does not require supports in structures, as this photocuring takes place in a liquid resin [15,16]. This technique offers advantages including a relatively low cost of the printer, compared with other 3D printers, a simple printing method, cost-effectiveness and high throughput fabrication. It is because that the printing speed of DLP relies on the height of the object to print in the Z axis, the size of the object in X-Y axis direction does not affect printing speed. Also, multiple objects can be printed on the same bed simultaneously without the need for additional printing time. With these benefits, DLP printing proved to be a promising method to fabricate 3D electrodes. One of the main reasons why DLP printing is not reported much for producing 3D electrodes is the limitation of material, which is related to the mechanism of DLP printing. DLP printing utilizes UV light to cure liquid resin consisting of a monomer, oligomer, and photo-initiator, and the irradiated pattern is polymerized, which converts shorter chain (monomer) into longer cross-linked chain (polymer), forming a 3D network by free radical polymerization. However, these resin materials are not usually conductive, and the final products are nonconductive polymers. Therefore, conductive materials for DLP printing have been required to print the electrodes. As an approach to develop a conductive 3D structure, composite materials which have combination of resin and conductive fillers have been introduced. Silver nitrate ( $\text{AgNO}_3$ ) with polyethylene glycol diacrylate (PEGDA)-based composite resin [17] ( $500 \text{ K}\Omega$ ) and multiwall carbon nanotubes (MWCNTs) with acrylic resin ( $2.7 \times 10^{-2} \text{ S/m}$ ) [18] ( $4 \times 10^{-6} \text{ S/m}$ ) [19] have been reported. Despite all these efforts, these electrical resistances are too high, or the conductivities are too low to use as a 3D electrode for supercapacitors. By solving these issues, DLP printing could be promising technology to fabricate 3D electrodes with the advantages such as 1) increase active material loading in unit area with minimum performance loss, 2) time-saving, cost-effective manufacturing in ambient operation environment 3) realization of tailorable complex electrode designs which can increase surface area or mechanical stability. 4) Adjustment of porosity by 3D design for electrolyte diffusion.



**Figure 1 Ragone plot for the various electrochemical energy conversion systems [1].**

## 1.2. Objective

The objectives of this thesis are designing and printing of 3D architecture electrodes for UV curing-based 3D printing technology to fabricate energy storage devices. The detailed objectives of this thesis are as follows.

- Design and optimization of photo-curable conductive resin (PCCR) for a digital light processing (DLP) based 3D printing method.
- Design of 3D Electrodes with a high surface area and mechanical durability.
- Characterization of 3D printed electrodes before and after pyrolysis.
- Fabrication of micro-supercapacitors and demonstration of their performance.

## 1.3. Contribution

- 1) Photo-curable conductive resins including acrylate with silver nanowire (AgNW) have been developed and optimized to use it in DLP 3D printing. To optimize photo-curable conductive resin, several parameters such as viscosity, the ratio of composition and light absorption of fillers have been considered. The optimized resins were evaluated by

confirming a printing quality of the complex model; octet unit cell.

- 2) As a novel approach, pyrolysis of DLP printed samples was performed. It was discovered that electrical resistance was significantly enhanced with maintaining the printed structures. Morphology and composition of pyrolyzed samples were analyzed to study those phenomena.
- 3) High aspect ratio electrodes consisting of truss structures have been designed to produce mechanically durable, high surface area 3D electrodes. 3D micro-supercapacitors were fabricated with gel type electrolyte. The performance of micro-supercapacitor was demonstrated and evaluated.

A journal paper has been published based on the research in this thesis:

S. Park, M. Kaur, D. Yun, and W. S. Kim\*, "Hierarchically Designed Electron Paths in 3D Printed Energy Storage Devices" *Langmuir*, **34**, pp. 10897-10904 (2018).

## **1.4. Thesis organization**

The organization of the thesis is as follows.

In Chapter 1, the motivation, objectives and contribution of this thesis are introduced. Chapter 2 introduces the literature review on recent development of various technologies to fabricate supercapacitors. Justifications of 3D printed electrode, instead of 2D, are presented. Chapter 3 explains a design and optimization of photo-curable conductive resin to be used in photo-curable 3D printer. The conductive resins consisting of a monomer, oligomer, photo-initiator, photo-absorber, AgNWs were studied to optimize the printing quality. The printing quality was evaluated by confirming printability of a highly complex model. In Chapter 4, design of 3D electrode and pyrolysis process are explained. The interdigitated electrodes consisting of truss unit cells are explained. The 3D printed electrodes are pyrolyzed and characterized. Chapter 5 demonstrates the micro-supercapacitor performance. Chapter 6 explains the conclusion and future work of this research.

## Chapter 2

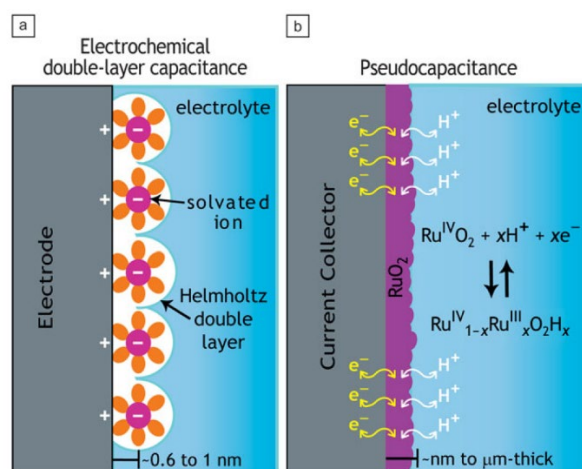
### Literature review

#### 2.1. Principle of supercapacitor

##### 2.1.1. Electric double layer capacitor (EDLC) & Pseudo-capacitor

The working mechanism of EDLC is storage of energy from the capacitance by electrostatic charge accumulation at the interfaces of electrodes/electrolytes. This charge accumulation comes from the separation of charges between the electrode and in electrolyte by  $\sim 6$  to  $10 \text{ \AA}$  of the electrical double layer, generating potential difference as show in Figure 2.1. Carbon-based materials such as activated carbon, carbon nanotube, activated carbon fibers [21] and graphene [22] have widely used for the electrode in the EDLC. However, carbon-based electrodes operated by electric double layer capacitance have low theoretical capacitance. To develop high-capacitance supercapacitors, pseudo-capacitors have been introduced, where capacitance comes from faradaic redox reaction of pseudo-active materials such as  $\text{RuO}_2$  [23],  $\text{MnO}_2$  [24],  $\text{NiO}$  [25],  $\text{Co}_3\text{O}_4$  [26], and conducting polymers [27]. The pseudo-materials having a high theoretical specific capacitance could enhance the performance of MSCs. For example, ruthenium oxide based the pseudo-capacitor has been proved 1200 F/g [28] while the graphene based EDLC demonstrated only 264 F/g [29].





**Figure 2.1. Schematic of charge storage via the process of either (a) electrochemical double-layer capacitance or (b) pseudo-capacitance [20]. Reprinted with permission.**

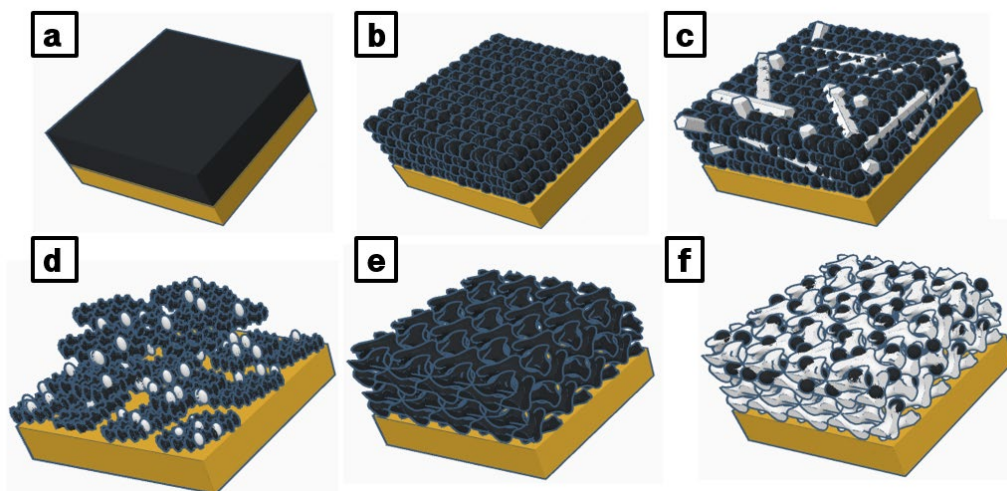
## 2.2. Development of micro-supercapacitor

### 2.2.1. Design of electrode

To enhance energy and power density of supercapacitors, the electrodes for MSCs need to fully facilitate both ionic and electronic current with a high specific surface area. Figure 2.2. illustrates electrode designs for MSCs. The conventional thick film electrode in Figure 2.2(a) depicts low ionic and electronic current path, where electrode/electrolyte involves EDLC or faradaic reaction only on the top surface. The bulk type electrode exhibit localized redox reaction on top of electrode surface. Especially, in this case, long ion diffusions and electron pathways through the active materials toward the current collector reduce efficiency of electrochemical reaction. Also, the electrolyte cannot be fully wetted within electrodes, resulting in limited ion diffusion into electrode materials. These inefficient and low surface area electrodes cannot achieve high energy and power density. To overcome these problems 3D nanostructured materials have been reported for MSCs electrode as shown in Figure 2.2(b). The numerous nanostructured materials such as nanoparticles, hollow spheres [30], nanowires [31], nanotube [32], nanosheets [33], nanoflowers [34] have been introduced. These 3D nanostructures materials synthesized by chemical oxidation/reduction could be formulated with liquid binders to produce a slurry. The slurry is coated on top of the current collector and dried to generate 3D nanostructure. In these electrodes, the gap between each nanomaterial offers a space for

electrolytes to be fully wet. The nanostructure having a high surface area could also increase energy density of MSCs. However, the high electrical resistance at the interface of each nanomaterial reduces the conductivity of the electrode system, resulting in low power output. As an approach to increase electrical conductivity of electrodes, high conductive nanomaterials have been used as an additive as depicted in Figure 2.2(c). The materials such as silver nanowires and carbon nanotube in the electrode offer superior electron pathway, which increase power density [35-37]. Although these electrodes with additives could have higher power output, there are still limitations. The electronic charge carriers still need to go through the interface of particles to be delivered to the current collector. These additional interfacial resistances resulting in poor electron transport cannot deliver charge carriers effectively. To avoid the interfacial resistance of nanostructure electrode, 3D structure by graphene sheets has been introduced as shown in Figure 2.2(d). Staking of the chemically reduced graphene sheet could form a randomly distributed 3D structure. The advantages of large-scale and low-cost synthesis of 3D graphene sheet have enabled this method to be feasible in MSCs electrodes [38-41]. However, the defects by impaired graphene in the chemical synthesis and fabrication process couldn't overcome the stability and conductivity limit. Moreover, in graphene stacking method, aggregation and strong  $\pi$ - $\pi$  interaction between each graphene sheet reduced the specific surface area. Also, the interfacial resistance between each graphene sheet reduces the conductivity of electrodes. To overcome this limitation, the researches on non-stacked 3D graphene material have demonstrated that pore volume and specific surface area can be significantly enhanced by unique 3D morphology of graphene [42]. However, the conductivity was still limited due to the interfacial resistance between each 3D graphene nanostructure. As a novel approach, 3D graphene structures by chemical vapor deposition (CVD) have been introduced to overcome previous limitation [43,44]. Although 3D graphene electrodes by CVD have proved high power/energy density in MSCs, the complex process, time consuming process and difficulty on handling CVD need to be improved. This may arouse researchers' interest in 3D interconnected monolithic structure with simple fabrication processes. The 3D interconnected structure without interfacial resistance gives a superior electron pathway for charge carriers. Also, the porous structure offers high surface area and enough space for electrolyte diffusion. The 3D interconnected monolithic structure having a higher conductivity such as silver can be used as current collector in Figure 2.2(e). To maximize electrochemical performance of MSCs, material selection and structural design can be considered in this electrode. The high conductive 3D interconnected structure with electrochemical deposition of

pseudo active material could be another strategy as shown in Figure 2.2(f).



**Figure 2.2. Design of 2D to 3D electrodes on current collector: (a) Thick film, (b) Nanostructured material, (c) nanostructured material + additive, (d) Graphene sheet with active material, (e) 3D monolithic electrode, (f) 3D monolithic current collector with active material.**

### **2.2.2. 2D planar micro-supercapacitor**

The 2D (planar) electrodes have been increasingly developed in past decades with numerous fabrication methods. Figure 2.3 depicts various approaches for electrode fabrication by 2D (planar) printing. Laser scribing technology is one of the promising methods in that it can produce the electrode with advantages of low cost, simple fabrication process, scalable and vacuum free. Figure 2.3(a) illustrates the fabrication of laser-scribed graphene-based MSCs. A standard light scribe DVD drive is used as a laser source to reduce graphite oxide to graphene. The produced graphene electrodes are mechanically durable, show high conductivity of  $1.7 \times 10^5$  S/cm with the high specific surface area  $1520 \text{ m}^2/\text{g}$  [45,46]. As another laser-induced technology, direct laser writing on polyimide(PI) sheets was demonstrated that it can produce macro-nanoporous carbon [47]. This technology is combined with organometallic materials to develop a sintered silver with high porosity as shown in Figure 2.3(b) [48]. Higher conductivity and high surface area generated by laser sintering of organometallic materials can be an adequate electrode for MSCs with simple and effective ways comparing to those MSCs reported

previously. The materials are not limited in silver because various organometallic materials can be synthesized and be used for direct laser writing. Ink jet printing is also well-known technology to produce MSCs. Various materials have been introduced for ink jet printing such as CNT/RuO<sub>2</sub> [49], and graphene [50]. Printing multiple layers is also possible with ink jet printing using graphene-based ink [51] in Figure 2.3(c) upper image. It is reported that it is possible to print entire MSCs cell by ink jet printing as shown in Figure 2.3(c) lower image. First, Cellulose nanofibers (CNF) are printed on A4 paper to enhance wettability of ink for following materials for MSCs. SWNT/AC with silver nanowire are printed on CNF to form electrodes. Finally, the electrolyte, with a photo-initiator is printed on the electrode and UV curing process is followed by to produce solid-state electrolyte [52]. One main advantage of these 2D printed MSCs is that the electrodes can be connected in series/parallel by computer design. This is important that the combination of series and parallel electrodes can increase the cell voltage and capacitance.

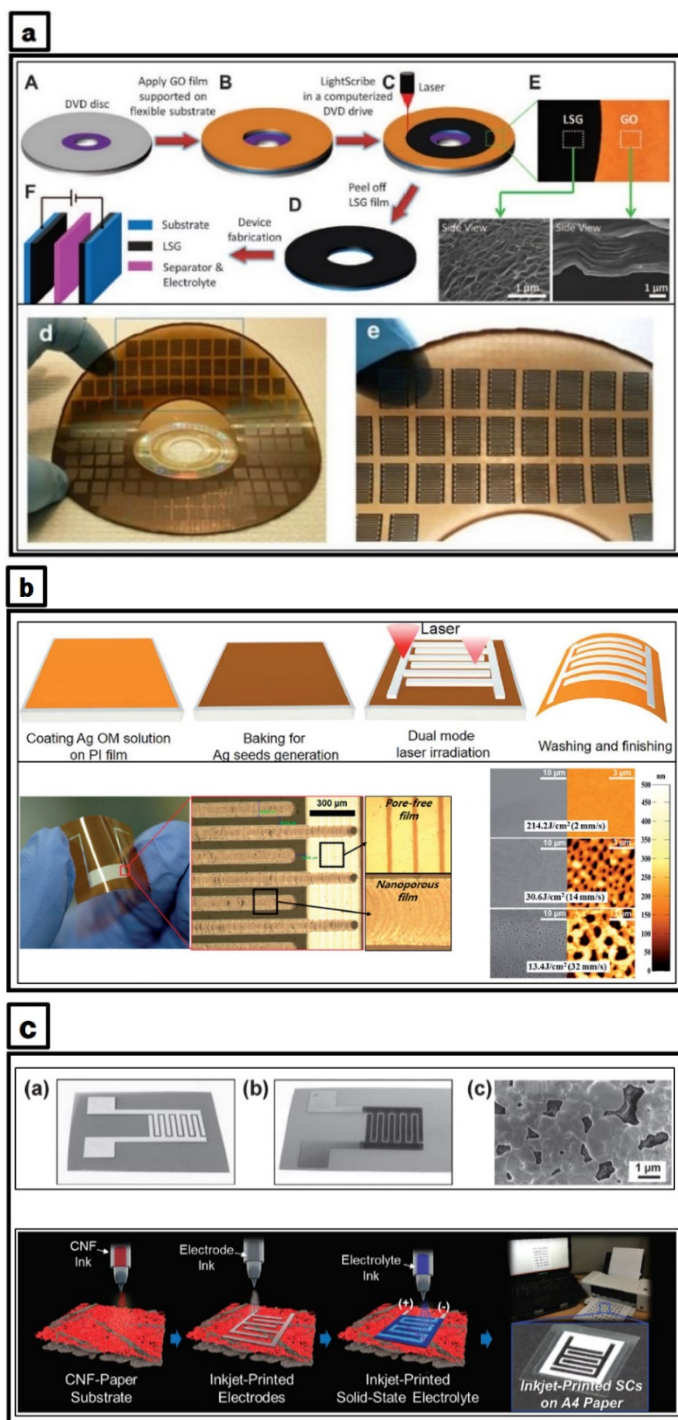


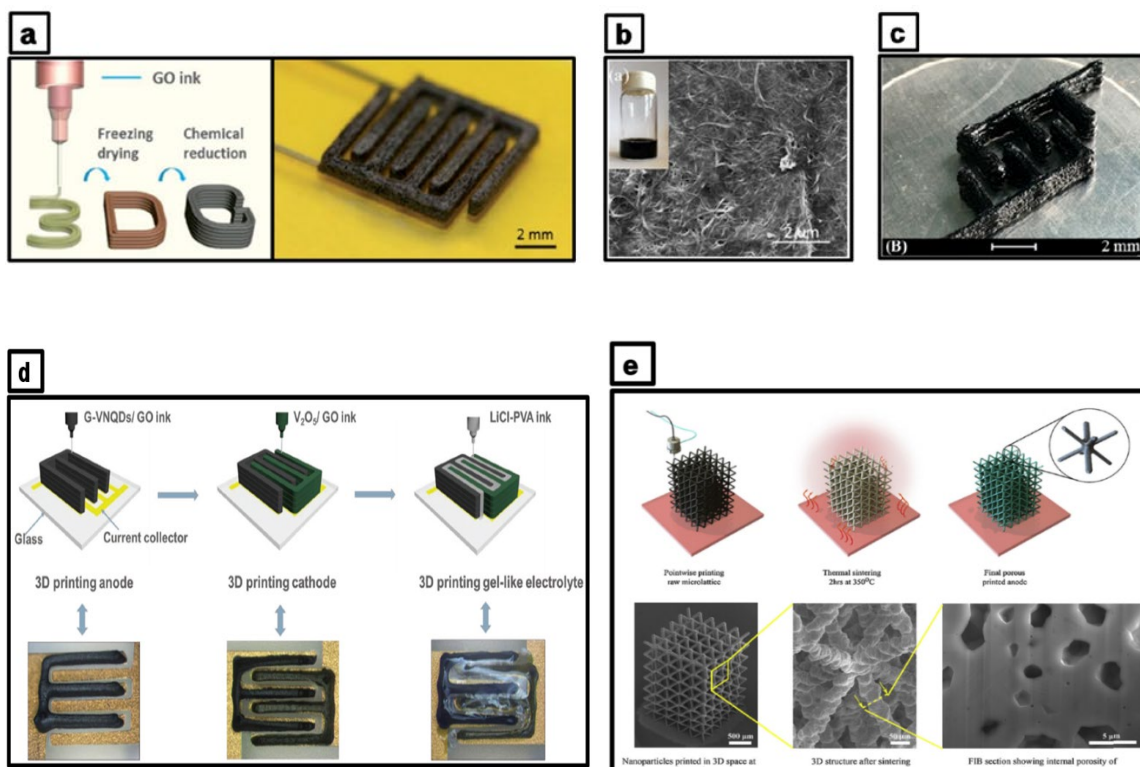
Figure 2.3. MSCs with Two Dimensional Electrodes by (a) laser scribing [45], (b) laser sintering [48] and (c) Ink-jet printing methods upper image: [51] lower image: [52]. Reprinted with permission.

## 2.2.3. Recent researches on 3D printed micro-supercapacitor

### 2.2.3.1. Extrusion printed 3D micro-supercapacitor

Extrusion printing (EP), or direct ink writing (DIW), is one of the most promising 3D printing methods with numerous advantages such as flexibility of material selection, low cost, simple printing process without post process. The flexibility of material selection on MSCs electrodes could be more emphasized because various materials having high surface area such as CNT, graphene and pseudo material also can be used. One prerequisite of the EP material is rheology study. The viscosity of EP material needs to be decreased as increasing shear rate, indicating shear thinning behavior. The applied force by extrusion reduces the viscosity of material and materials return to original state when it comes out from the nozzle. This is important that increase of viscosity can make the printed structure maintain. This can be more explained by shear elastic modulus and loss modulus as a function of shear stress. At lower shear stress, plateau shear elastic modulus ( $G'$ ) that is higher than its viscous modulus ( $G''$ ). This explains that materials can sustain its shapes and their wetting/spreading effects are minor. Moreover, at higher shear stress, shear elastic modulus ( $G'$ ) is slightly smaller than loss modulus ( $G''$ ) which means when the stress is applied to material in extrusion nozzle during 3D printing, materials flow and spread out easily by exceeding the shear yield. And, when material is exposed to ambient air through the nozzle, at low shear stress, materials quickly stiffen as it returns to a quiescent state. The extrusion 3D printed MSCs are described in Figure 2.4. One of the popular materials for EP is graphene, which has demonstrated high electrochemical performance. By adopting these materials with 3D printing (EP), it shows synergy effect because of both the advantage of 3D printing and electrochemical performance of graphene materials. The related research with this is described on Figure 2.4(a) [53]. The inks consisting of graphene oxide (GO) with DI water are printed on current collectors of Cr/Au deposited on polyimide film. After 3D printing, structures were freeze-dried for 12 h at the temperature from -50 °C to 20 °C. The result reveals that the printed electrode at different freeze-dry temperature shows difference in porosity and conductivity, resulting in different capacitance. Finally, the freeze-dry electrodes with high porosity were reduced with hydrazine hydrate in a vacuum desiccator at 90 °C for 3 h and vacuum dried at 100 °C for 3 h 50 to form a graphene structure. A disadvantage of this printing method is that it is performed in quite toxic environment by using hydrazine hydrate. The whole process is time-consuming and complex steps to generate final

graphene electrodes. Similar ways, carbon nanotube by EP is reported [54,55]. Dispersant agent, IPA, EG, CNT power (8 wt%) were prepared and printed by air-powered dispenser. The printed interdigitated electrodes were dried at 120 °C to remove the solvent overnight in a vacuum oven. Carbon nanotubes (CNTs) having high electrical conductivity and a high specific surface area with EP are a candidate of MSCs electrodes in Figure 2.4(b). A literature reported graphene/PANI materials with EP [56] in Figure 2.4(c). PANI (Polyaniline) is a conductive polymer used as pseudo materials for the pseudo-capacitor. The combination of graphene and PANI materials have been demonstrated high specific capacitance of 1341 F/g at 0.5 A/g by exhibiting high conductivity, high specific surface area and highly active electrochemically reaction of PANI. The EP with this graphene/PANI also demonstrated 1329 mF/cm<sup>2</sup> of high areal capacitance by having the high aspect ratio. The EP based 3D printing is usually possible to print only the electrodes. However, not only electrodes but also electrolytes can be printed with EP as shown in Figure 2.4(d) [57]. Vanadium pentoxide (V<sub>2</sub>O<sub>5</sub>) with GO and graphene–vanadium nitride quantum dots (G–VNQDs) with GO were printed to fabricate asymmetric MSCs. The electrolyte, LiCl with polyvinyl alcohol (PVA), was also printed to fabricate quash-solid type MSCs.



**Figure 2.4. Directly Written MSCs: Extrusion printing with (a) reduced graphene oxide [53], (b) CNT [55], (c) graphene/PANI [56], (d) V<sub>2</sub>O<sub>5</sub> + GO, G–VNQDs + GO, LiCl with PVA. (e) Aerosol jet printing (AJP) with Ag nanoparticle [61]. Reprinted with permission.**

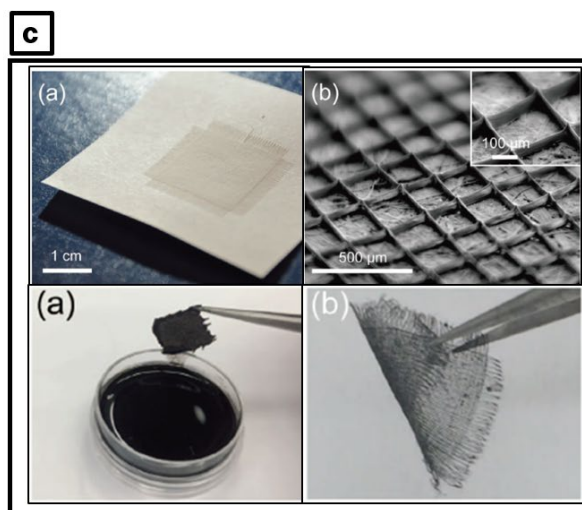
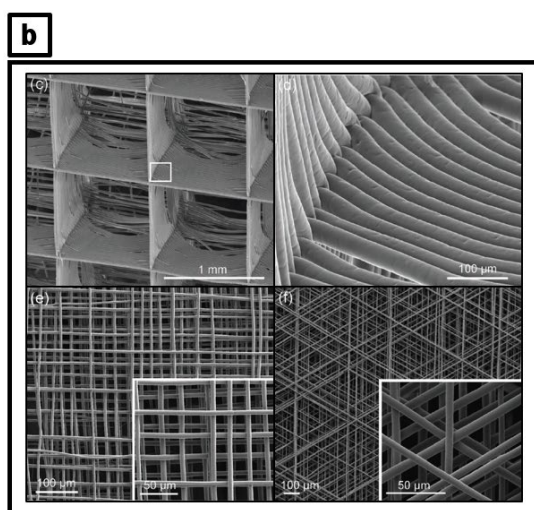
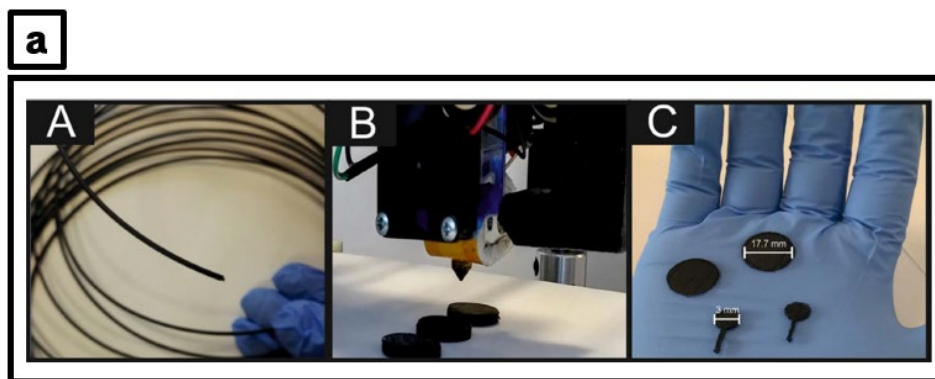
Although extrusion printing has widely used to produce 3D electrode, there is a critical limitation; clogging issue. The solid contents in solvents clog in nozzle as time goes, resulting in interrupting constant flow of the materials. As an advanced EP technology, Aerosol jet printing (AJP) could be appropriate to improve this issue. In AJP, functional inks are aerosolized and flow with carrier gases. The mechanism of producing aerosol is classified into pneumatic and ultrasonic. The aerosol materials are directly printed through a nozzle by a coaxial sheath gas flow [58,59]. Recently, it is demonstrated that AJP have printed high resolution (20  $\mu\text{m}$ ) 3D architecture with ability to control porosity in the architecture [60]. With this printing method, 3D electrodes for micro-battery have been successfully fabricated in Figure 2.4(e) [61]. The conductive 3D hierarchical structures also could be applied in MSCs electrodes. The high surface area from hierarchical structure increases the capacitance of MSCs by having higher EDLC and vigorous electrochemical reaction. The high conductivity can also transport the electrons effectively.



### **2.2.3.2. FDM / Electro spun printed 3D micro-supercapacitor**

Fused deposition modelling (FDM) is another well-known 3D printing system. A research group has reported sandwich type supercapacitor by FDM printing [62] in Figure 2.5(a). The filament composed of 8 wt% graphene and with 92 wt% PLA were successfully printed and used as coin type electrode. The fabricated supercapacitors with solid type electrolyte have proved capacitive behavior of 10.46  $\mu\text{F}$  at 10  $\mu\text{A}$ . Although the printed electrodes are a simple shape of disks in this paper, it is capable to print more complex structure or interdigitated electrode by FDM. Also, the filaments can be produced with different material combination. It means that other active materials for MSCs can be applied. However, there will be a threshold to increase solid contents in the thermoplastic matrix as the high contents of solid filler make filaments brittle, which have difficulty to produce filaments. The brittle filaments also influence on filaments feeding process, where the constant feeding cannot be performed, resulting in low printing quality. Also, thermoplastic based materials may be melted at high temperature above 200  $^{\circ}\text{C}$ . This restricts MSCs operation in high temperature.

It could be controversial to consider electro-spinning-based printing as a 3D printing. Nevertheless, it could be categorized in 3D printing in futuristic aspect. The reported articles have demonstrated 3D lattice structures by electro spinning printing [63-66]. The line width can be controlled by spinneret diameter, voltage, collector distance and temperature. The line width can be reduced up to  $817 \pm 165$  nm in Figure 2.5(b). Based on this, another paper demonstrated electro spinning printed supercapacitor with 5 $\mu\text{m}$  width grid pattern with 50 layers [67] in Figure 2.5(c). The 3D grid patterns serve as scaffold for active material. CNT ink was deposited on the grid scaffold by simple dip coating process. The printed line width can be controlled by the motion speed and applied voltage. In this paper, grid patterns are printed by moving the substrate instead of moving a nozzle. However, it will be possible for the nozzle to move into X, Y, Z direction as the conventional EP prints. More importantly, the electro spinning process with the extrusion-based process can print ultra-high resolution. The surface area of electrodes can be increased with the electrodes consisting of 1D fiber materials. However, the materials are limited in polymer and conductive materials for this printing are not investigated much. The printability of the pseudo materials, or electrically conductive materials needed to be more studied to achieve higher capacitance and to be feasible electrodes in MSCs.



**Figure 2.5. FDM, Electro spun printed 3D MSCs: (a) FDM printing with graphene + PLA [62], (b) Electro spinning printed 3D structure [63] and (c) 3D electrode [66].**

### 2.2.3.3. Binder Jet Printed, Laser Processed 3D micro-supercapacitor

BIJ printing is a 3D printing technique where precursor materials are used in a dry form consisting of nano to macro size particles. The patterns can form with a binder which serves as 'glue' making the powder stick together and generates a layer. This builds a 3D structure by a successive process of feeding a powder layer and applying binders with designed 2D design. A group fabricated supercapacitor electrode by BIJ [68] as shown in Figure 2.6(a). First, the synthesized graphene oxide (GO) was treated by the process of thermal expansion and reduction to produce thermally reduced graphene oxide sheets. The binder consisting of >90 % water, 8 % glycerol and 2 % other humectants were used to print the electrodes. Palladium nanoparticles, <9 wt% were infiltrated into BIJ printed electrode to reduce the contact resistance of the graphene powers. Specific capacitance was achieved up to ~260 F /g and ~700 mF /cm<sup>2</sup>, respectively at 5 mV/s in 1 M H<sub>2</sub>SO<sub>4</sub> electrolyte. The cycling test results indicate that the capacitance can be retained 80 % over 1000 cycles. Figure 2.6(b) depicts fabrication process of SLM printed electrodes for MSCs. SLM printing, A laser melts metallic powder selectively and to form a 2D to 3D structure [69], has been used to build interdigitated 3D electrodes for MSCs [70]. Titanium alloy using Ti<sub>6</sub>Al<sub>4</sub>V powder was printed by SLM. Polypyrrole, conductive polymer or/and pseudo material, was coated on the printed electrodes by electrodeposition method to enhance electrochemical performance. The electrochemical characterization of fabricated supercapacitor with PVA-H<sub>3</sub>PO<sub>4</sub> electrolyte reveals that the areal capacitance was 0.057 F /cm<sup>2</sup> at a scan rate of 20 mV/s and 90 %, 78 % capacitance retention at 500, 1000 cycles respectively. Another group has successfully demonstrated a supercapacitor composed of PANI deposited Fe-Ni alloy electrode and Na<sub>2</sub>SO<sub>4</sub> as an electrolyte with SLM printing [71].

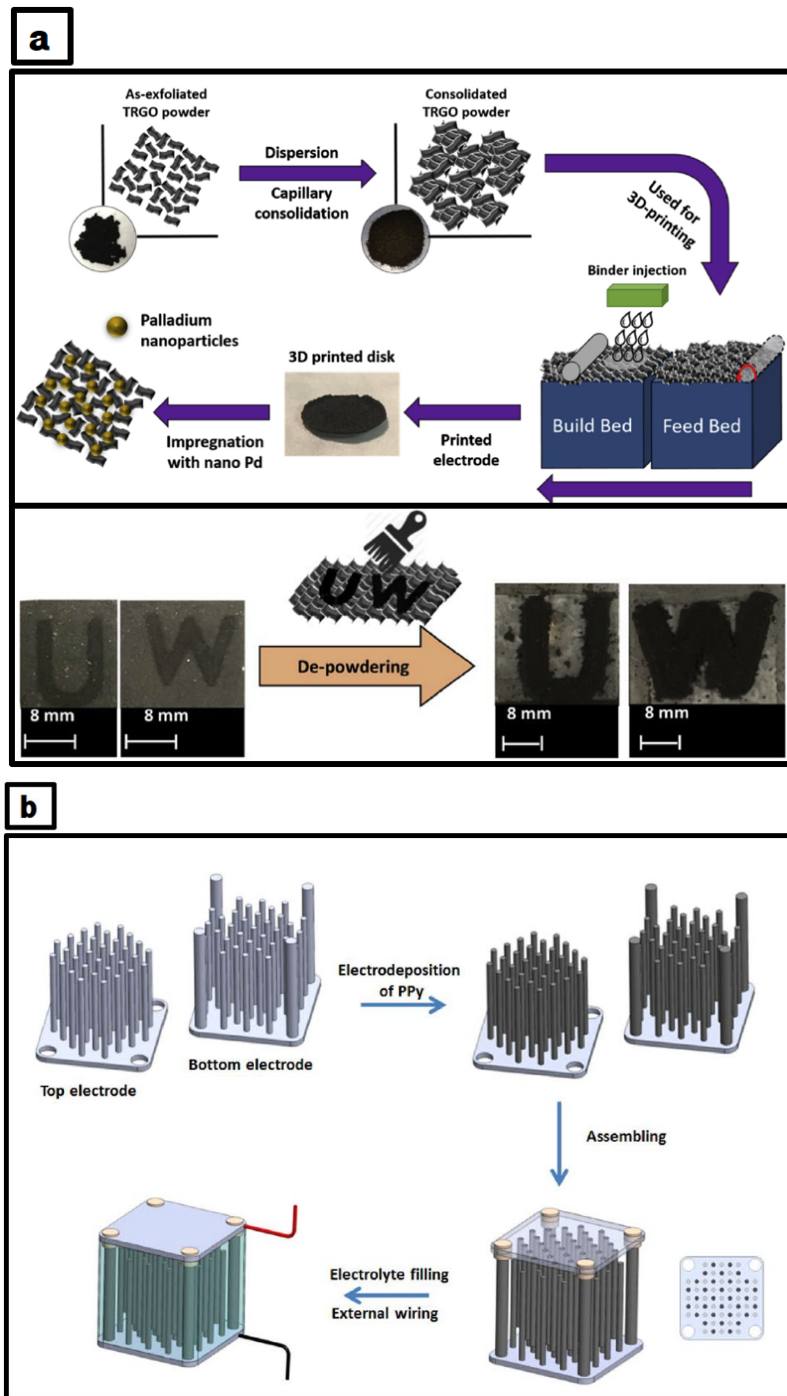


Figure 2.6. Binder ink Jet Printed, Laser Processed 3D MSCs: (a) BIJ with graphene [68], (b) SLM with  $Ti_6Al_4V$  powders [70]. Reprinted with permission.

## **Chapter 3**

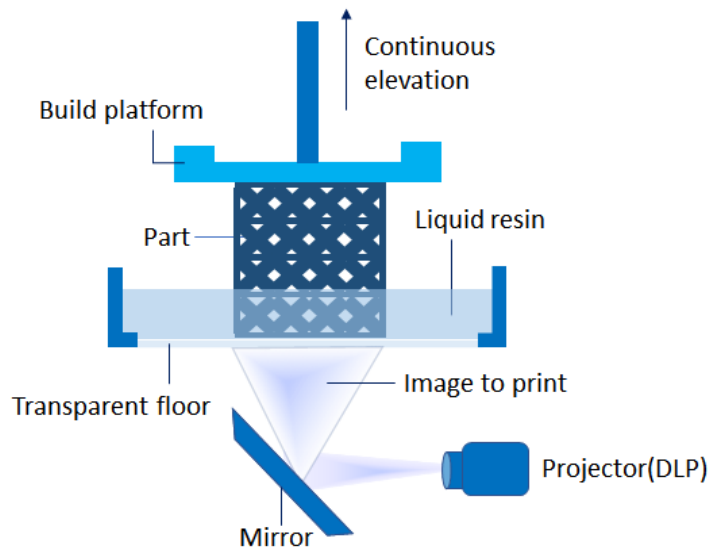
# **Design and Optimization of photo-curable conductive resin**

### **3.1. Objective and Plan**

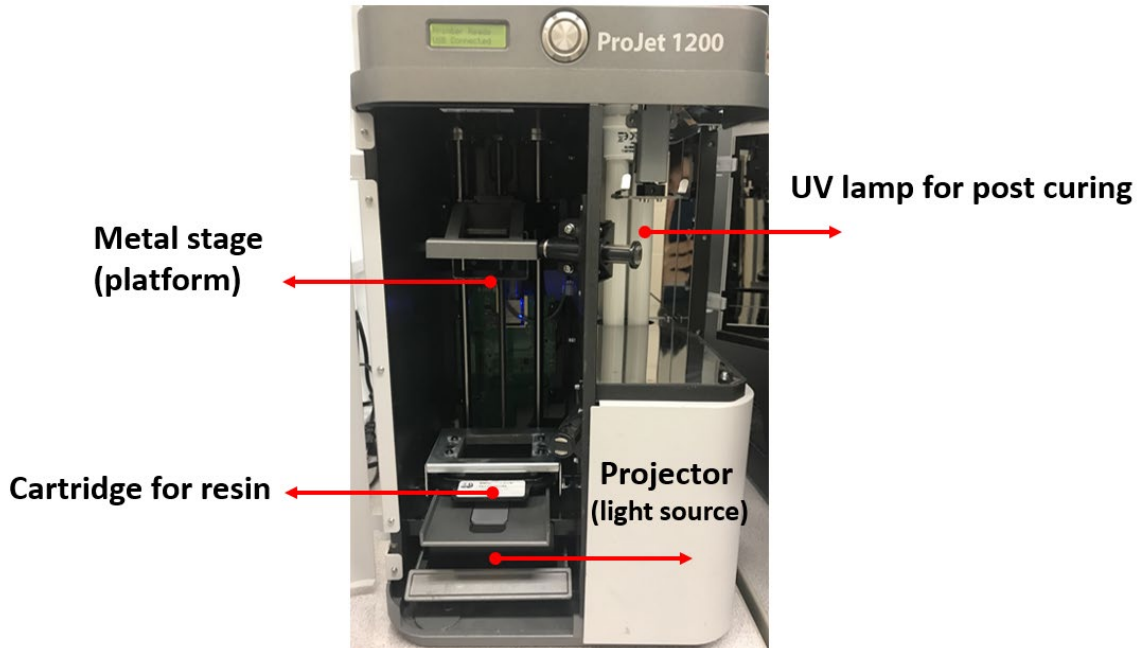
The objectives on design and optimization of photo-curable conductive resin are to develop suitable materials for DLP printing. First, the photo-curable resin for DLP printing is designed to be solidified quickly and having high electrical conductivity. Second, the photo-curable conductive resin is optimized by considering the viscosity and photo-absorbing effect.

### **3.2. 3D printing process**

DLP 3D printing technology means 3D printing by Digital light processing with stereo lithography technology. The UV light (about 400nm wavelength) from projector cures resin materials layer by layer made up with oligomer, monomer and photo-initiator. A platform, where printed object appear, moves up side every a few seconds to cure next layer from liquid resin to rigid polymer (Figure 3.1). In this thesis, A DLP printer (ProJet 1200) from 3D Systems has been used for all the printing experiments as shown in Figure 3.2. The cartridge in which the resin material is loaded is in Appendix A. The reported resolution of the 3D printer is  $585 \times 585$  dpi ( $56 \mu\text{m}$ ) and each layer height is  $30 \mu\text{m}$  using a LED projector at 405 nm wavelength [72]. The test result of resolution experiment in X, Y axis is also available in Appendix B. The 3D structures were printed by the DLP printer and rinsed by isopropyl alcohol to remove unreacted resin residues and dried in the air overnight. The post curing process was conducted with a built-in UV lamp (Osram Dulux L BL UVA 18W/78 2G11) inside the DLP printer, a wavelength of about 400 nm, and an irradiance of  $1350 \mu\text{W}/\text{cm}^2$  to increase the polymerization conversion rate and to terminate polymerization of activated resin, which results in improved mechanical properties [73].



**Figure 3.1. Schematic of DLP printing system**



**Figure 3.2. Photograph of DLP printer, ProJet 1200 from 3D systems.**

### 3.3. Composition of photo-curable resin

Photo-curing is a polymerization process from liquid resin to solid material under the light at certain range of wavelengths. The photo-curable resins usually contain four major components: monomer, oligomer, photo-initiator and photo-absorber.

#### 3.3.1. Monomer

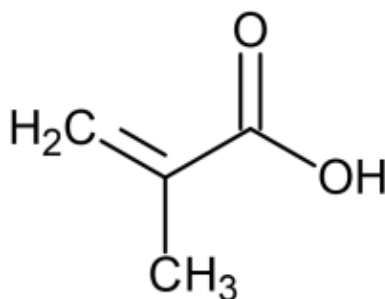


Figure 3.3. Chemical structure of methacrylic acid

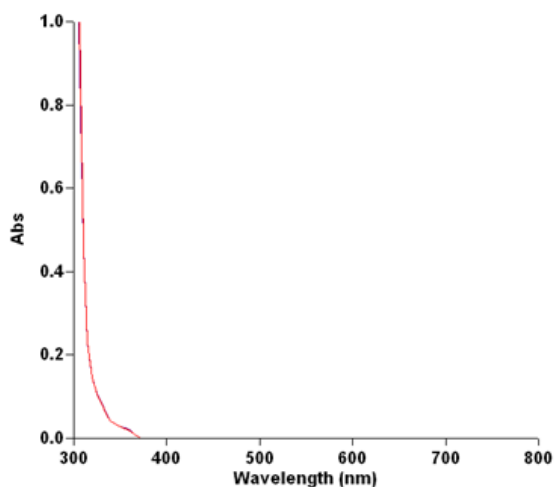


Figure 3.4. UV-VIS spectra of MA

Monomers are low organic molecules that can be a basic unit of a polymer. Monomers can form chemical bonds with another monomer and finally become a polymer. When only one type of monomer is used, the polymer is called homopolymer and when two types of monomer are used, it is called copolymer [74]. Also, usually, as the viscosity of monomers is low, it can be

used to optimize the viscosity of photo-curable resin. In my work, Methacrylic acid (MA), depicted in Figure 3.3, is used as a monomer. UV-Vis spectroscopy test was performed to analyze light absorbance of MA materials. This determines the absorption of the samples at the range of wavelengths. The wavelength was set from 300 to 800 nm (X axis). The absorbance in Y axis measures how much light does not pass through the materials. In Figure 3.4, Around 400 nm wavelength, which is the same range in DLP light source for polymerization, there is no light absorbance. It indicates the light at the 400nm wavelength can pass through MA material and deliver the light source into the resin effectively.

### 3.3.2. Oligomer

Oligomers are more complex molecules than monomer. It consists of a few monomers. When the oligomers are composed of two, three and four monomers, it is called dimers, trimers and tetramers, respectively [75]. In my work, aliphatic urethane tri-acrylate as shown in Figure 3.5 is used as an oligomer.

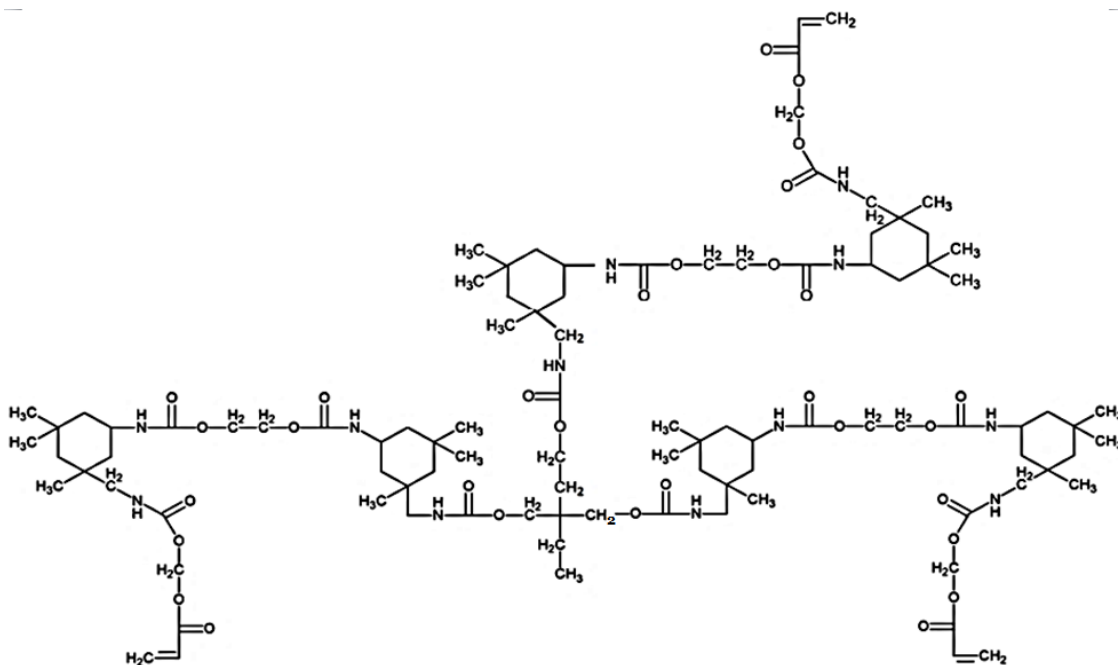


Figure 3.5. Chemical structure of UTA



### 3.3.3. Photo-initiator

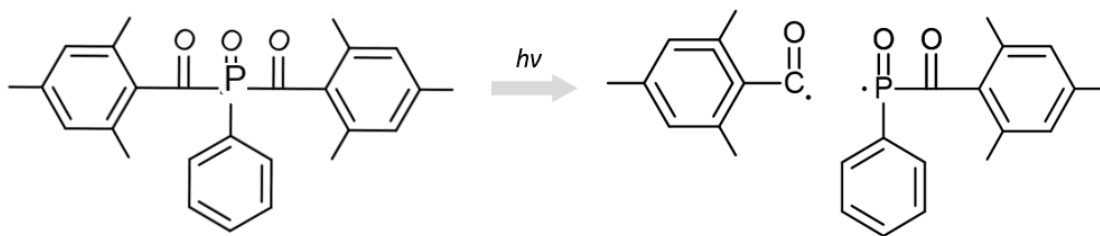


Figure 3.6. Chemical structure of Irgacure 819 before and after fragmentation

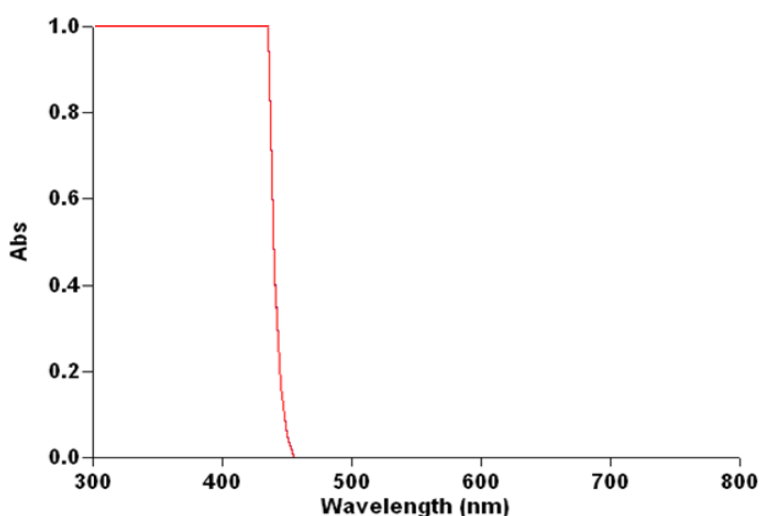


Figure 3.7. UV-VIS spectra of Irgacure 3w% in MA

Photo-initiators are components to trigger photo-curing. It absorbs lights and thereby undergoes fragmentation of bond and generates free radicals, which are the species of initiating polymerization. It is important to select appropriate photo-initiators for specific applications as they have different light absorption range. For example, UV curable resin contains photo-initiator which can absorb UV light (250nm~400nm). In this experiment, Irgacure 819; Bis(2,4,6-trimethylbenzoyl)-phenylphosphineoxide is used as photo-initiator. The chemical structure of Irgacure 819 is in Figure 3.6. The UV-VIS spectra in Figure 3.7 demonstrates the light absorption in the wavelength range of  $< 450\text{nm}$ . This is important that the 3D printing light source (DLP projector) has 400nm wavelength, which corresponds to the photo-initiator absorbance wavelength.

### 3.3.4. Light induced polymerization

Photo-curable resins consist of monomers, oligomers and photo-initiators. When lights were illuminated, free radicals are generated in photo-initiator. In an initiation step, the radicals react with the double bonds (-C=C-) of the monomer, oligomer [76] resulting in radical formation in monomers and oligomers. In the propagation step, the radicals in oligomers and monomers react with additional oligomers and monomers, resulting in new radical's formation in another monomer/oligomer. This process propagates, generating a longer chain. Finally, the propagation stops once all radicals are used in the reaction. This is called termination. The three steps finally make a high molecular cross-linked 3D network. As this highly cross-linked molecular has rigid property, it shows solid structures. In the 3D printing system, the resin in the vat is polymerized layer by layer by this mechanism. The 2-dimensional images, which are the light source by the projector, are illuminated in the resin successively. The accumulated 2D layers finally produce a 3D object.

### 3.3.5. Photo-absorber

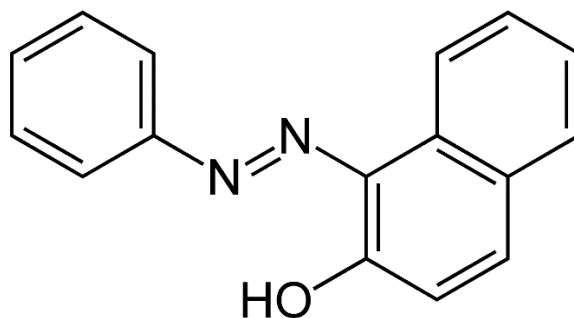
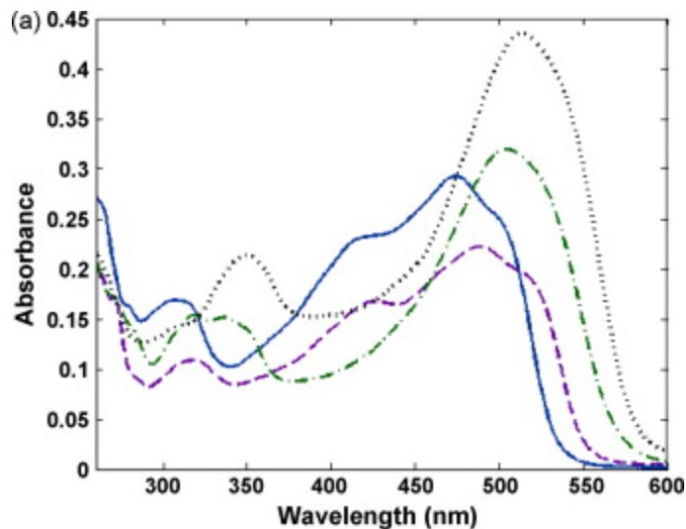


Figure 3.8. Chemical structure of Sudan I



**Figure 3.9. UV-VIS spectra of Sudan I (solid line) [77]. Reprinted with permission.**

Photo-absorber, Sudan I (Figure 3.8), is used in these experiments to enhance the printing quality in terms of resolution and roughness. Photo-absorbers absorb the light in certain range of wavelengths and dissipate the absorbed energy into heat [78]. This limits the curing depth accordingly and increase the threshold of light flux required [79]. In this process, light absorption in photo-absorber can inhibit the light absorption in photo-initiator. In this reason, photo-absorber is sometimes called photo-inhibitor. The main advantage of photo-absorber is that it can enhance the resolution and roughness by preventing from over curing of resin and by adjusting curing depth [80]. Additionally, as the photo-absorbers absorb unwanted light before or after printing process, the stability of the photo-curable resin could be increase, resulting in longer material preservation. Sudan I is selected in this experiment because it has strong light absorption in LED range (>400nm) as shown in Figure 3.9 so that the photo-initiator we choose can be only sensitive below 400nm.

### 3.4. Printing quality on different ratio of the resin composition

Table 3.1 demonstrates printing resolution with respect to different parameters. The ratio of oligomer and monomer (O:M), printable strut (Figure 3.10) width, concentration of photo-absorber and curing time (5.5s, 8.5s) are considered. A complex truss structure, *octet*, is selected to study the printing resolution. The samples are printed by DLP and washed by isopropyl alcohol (IPA) for 2 min, followed by post curing process for 15 min to print high contrast and well-defined structures. In the preparation of the DLP printable resin, the viscosity of the composite resin is an important parameter. It is easier to wash out unreacted resin when we use low viscosity materials. More importantly, if the viscosity is too high, the resin cannot fill in between the printed layer and the bottom of the cartridge in time, making an empty space as shown in Figure 3.11. The percentage of monomer needs to increase so that the prepared resin has a low viscosity. Viscosity of oligomer and monomer is 35000 mPa.s and 1.54 mPa.s respectively. The ratio between oligomer and monomer (O:M) was set as 2:8 3:7, 4:6, and 5:5. The results explain that, overall, the structures with Sudan I have higher resolution than the structures without Sudan I. Specially, the samples with 0.05% of Sudan I (Table 3.1j,k,l) show that the core of the structures is fully defined without over curing. The effect of O:M ratio without sudan I in Table 3.1a,d,e doesn't show significant difference although higher oligomer contents, 5:5 (Table 3.1e), results in somewhat lower resolution. This is because that higher functionality in oligomer accelerates the curing reaction [81]. In detail, the resins containing higher percentage of the oligomers, which have higher functionally, results in over curing in a same curing time. Printing was not successful with 2:8 ratio of O:M due to insufficient polymerization due to lower contents of oligomer. The printing with 3:7 ratio with Sudan I was not successful both 0.02 and 0.05 % of Sudan I by insufficient polymerization due to too much light absorbing effect of Sudan I. To study minimum printable strut size, 300 $\mu$ m, 400 $\mu$ m and 500  $\mu$ m were set. The results show that the minimum strut size of the complex structure in this experiment is around 400 $\mu$ m. The structures with 300 $\mu$ m strut size were not successfully printed (Table 3.1b,f). Moreover, the 300 $\mu$ m strut samples are degraded easily during cleaning processes in IPA. In the Table 3.1h and i, short curing time (5.5s) produces a higher resolution showing more defined structure than that of 8.5s curing time at 0.02 Sudan I %. However, at higher Sudan I (0.05%), 5.5s curing time produces a structure with some defects as shown in Table 3.1k in circle while structure printed by 8.5s curing shows perfect structure without any defects. This is

because that at higher Sudan I concentration, 5.5s curing time is not enough for resin polymerization due to the photo-absorbing effect of Sudan I. The 5:5 resin with Sudan I was not tested because we initially designed low viscosity materials for DLP printing. In conclusion, the optimized resin condition by DLP printing is at 4:6(O:M) with 0.05% Sudan I and 8.5 s curing time.

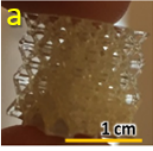
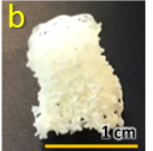
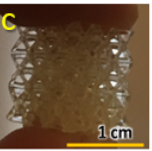
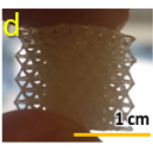
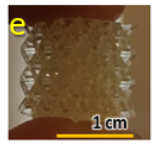
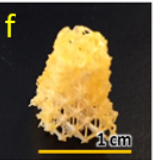
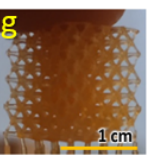
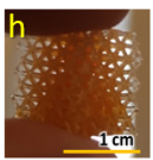
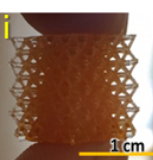

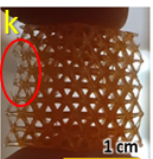
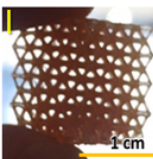
O:M \ Sudan %	3:7	4:6				5:5
	500 $\mu$ m	300 $\mu$ m	400 $\mu$ m	500 $\mu$ m		500 $\mu$ m
	8.5s	8.5s	8.5s	5.5s	8.5s	8.5s
0%						
0.02%	X					
0.05%	X	X				

Table 3.1. Photographs of DLP printed octet structures with different parameters

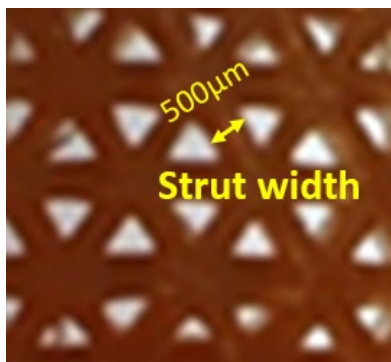
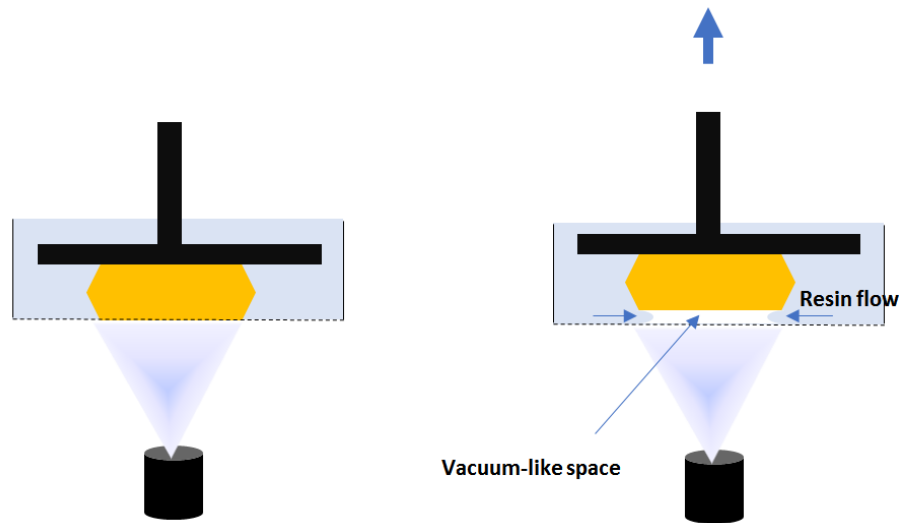


Figure 3.10. photograph of octet structure showing 500 $\mu$ m strut width



**Figure 3.11. Schematics of resin flow during DLP printing**

### 3.5. Mechanical testing

Although adding Sudan I, photo-absorber, to resin can enhance printing resolution, the mechanical property of DLP printed octet structures could be different. To study Sudan I effect on mechanical property, compress test was performed. Octet structures in a dimension of 1.5 cm x 1.5cm x 1.5 cm with 500 $\mu$ m in strut width were printed by using the photo curable resin (PCR) without Sudan with Sudan I. Compress test under 2mm/min compress speed was conducted by mechanical testing machine, EZ-LS long-stroke model, from SHIMADZU. The graph in Figure 3.12 illustrates that PCR has high higher ultimate tensile strength than that of PCR with Sudan I. It can be explained that Sudan I in PCR absorbs the light and the resins are partially polymerized, resulting in lower ultimate tensile strength. Interestingly, PCR with Sudan I show four different peaks as the strain increase. These peaks could correspond to the number of octet unit cell in Z direction. Numerous noises in the graph of PCR with Sudan I explain that the struts in the octet structure are collapsing. Unlike PCR with Sudan, octet printed with PCR shows more catastrophic failure at once, showing a peak around 0.13 strain. The stress is well distributed into the structures under compress load. Once it exceeds the yield point, it collapses entirely at around 0.15 strain.

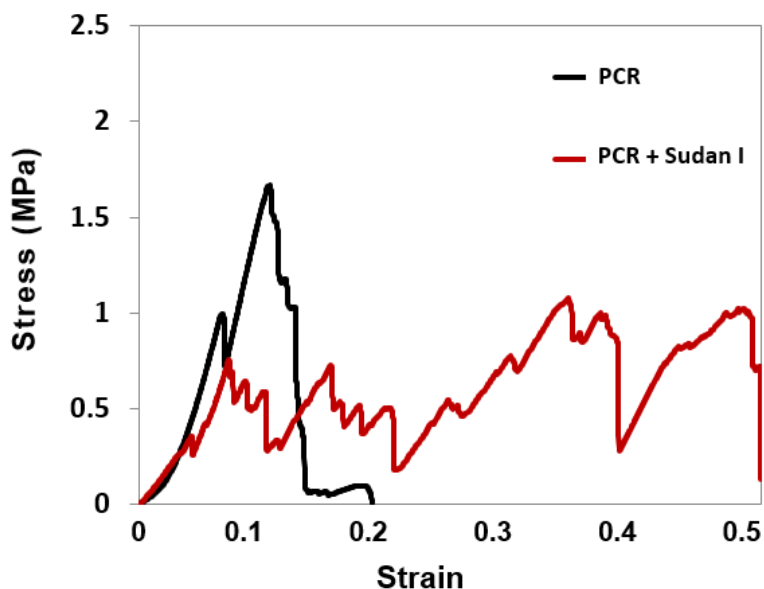


Figure 3.12. Stress versus strain graph under the compress test

### 3.6. Design of photo-curable conductive resin

The photo-curable resin and polymerized resin by DLP are not conductive. To achieve high conductivity to fabricate 3D electrode, AgNWs are selected as conductive filler to make photo-curable conductive resin. In the light induced polymerization process, high contents of additives in the photo-curable resin could reduce the polymerization due to light absorption [82]. This needs to be more considered when black pigments are used because it absorbs the light in all the range of wavelengths. In this reason, AgNWs are appropriate material as it has low percolation threshold; it has high conductivity in composite at low concentration of AgNWs. It is demonstrated that AgNWs/polystyrene nano-composites have a percolation threshold at 2.3vol% of silver, showing  $10^{-3} \Omega \cdot \text{cm}$  [83]. It is also introduced that AgNWs in carboxymethyl cellulose (CMC)-matrix have proved a percolation threshold in at 0.29 vol. with an electrical resistivity around  $10^{-3} \Omega \cdot \text{cm}$  by high aspect ratio of AgNWs [84]. Low concentration of AgNWs in composites is more important in DLP system as the light for polymerization needs to be delivered to the photo-curable resin. In this experiment, AgNWs were synthesized by a large-scale polyol method with dimensions of AgNW as 50 nm in diameter and 10  $\mu\text{m}$  in length, respectively [85]. The photographs of the synthesis images and optical microscope image of AgNWs as synthesized are in Appendix C.

### 3.6.1. Viscosity optimization

In the preparation of the 3D printable resin, the viscosity of the composite resin is an important parameter. If the viscosity is too high, the resin cannot fill in between the printed layer and the bottom of the cartridge in time, making an empty space. This phenomenon causes missed layers or entire printing failure while the object is printing. However, if the viscosity is too low, AgNW fillers could be segmented during printing, which induce a gradient concentration of AgNWs inside of the resin, due to the gravitational force against the buoyancy of resin and friction force [86]. To calculate the velocity of segmentation of silver fillers, Stokes law can be used, which is defined as follows: eq1

$$v = \frac{2(\rho_c - \rho)d_c^2 g}{9\eta} \quad (1)$$

where  $\rho_c$  is the density of the particle,  $\rho$  is the resin density,  $d_c$  is the particle diameter,  $\eta$  is the solution viscosity, and  $g$  is the gravitational acceleration. However, as Stokes law can analyze segmentation of “spherical particles”, only silver nanoparticles, as a minor product during AgNWs synthesis, are applicable with this equation. On the other hand, segmentation velocity of AgNWs can be different from that of spherical particles due to the high aspect ratio of AgNWs which have anisotropic behavior in resins. Another model for the calculation of segmentation velocity of nanowires is reported below: eq2 [87]

$$v_s = g \times (\rho_P - \rho) V \frac{[\ln(\frac{l}{d}) - 0.81]}{2\pi Y \mu l} \quad (2)$$

where  $g$  is the gravitational acceleration constant,  $\rho_P$  and  $\rho$  are the densities of nanowire and fluid, respectively,  $Y$  is the drag correction factor,  $V$  is the volume of the NW,  $d$  is the diameter of the NW,  $l$  is the length of the NW, and  $\mu$  is the viscosity of the solution. In both eqs 1 and 2, the viscosity is inversely proportional to the segmentation velocity of the NWs. In other words, high viscosity materials can impede the segmentation of NWs during the printing process. For this reason, the photo-curable resin was designed to have relatively high viscosity: 1300 mPa·s of viscosity at 25 °C. Monomer (35 wt %), oligomer (65 wt %) and initiator (3 wt % of the resin) are



formulated to make this viscosity. Although this viscosity is much higher than that of conventional resin with poly(ethylene glycol) diacrylate (PEDGA) for DLP printing (~100 mPa·s) [88], the printed 3D architecture with the developed resin did not affect its printing quality, and there is no noticeable sedimentation of AgNWs in the resin while printing.

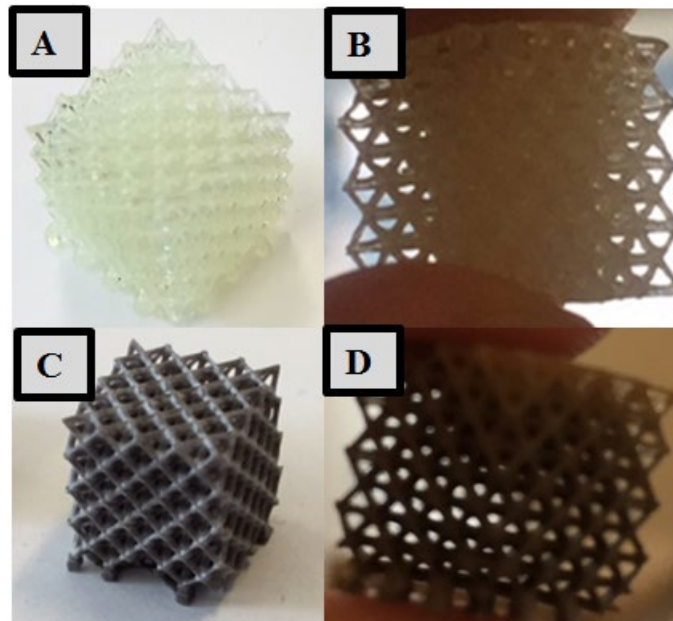
### 3.6.2. Light absorbing sensitivity

Another important component for better printing quality, especially for a 3D-complex structure, is the photo-absorber, which is widely used in DLP printing to adjust curing depth and width by inhibiting polymerization accordingly and resulting in printing detailed features [89,90]. However, without a photo-absorber, the printed micro-truss structure (octet unit-cell 4 × 4 × 4) made with the designed photo-curable conductive resin showed well-defined structure (Figure 3.13) as designed by 3D modeling. It is attributed to the light-scattering or absorbing effect [91] of AgNWs serving as photo-absorber to prevent over curing of octet structure. Similarly, as a supporting reference, TiO<sub>2</sub> nanoparticle-based photo-curable composite having a high refractive index has been introduced to adjust Z-axis resolution and the surface details [92]. A similar phenomenon with silver nanoparticle-decorated Pb(Zr,Ti)O<sub>3</sub> micro-particles has also been reported [93]. This can be explained in detail by Jacob's equation (eq3) [94] as shown below:

$$C_d = D_p \ln \left( \frac{E}{E_c} \right), D_p = \frac{2d_{50}n_0^2}{3Q\Delta n^2} \quad (3)$$

where  $C_d$  is the curing depth,  $D_p$  is the resin sensitivity,  $E$  is the energy density of incident light,  $E_c$  is the critical energy density,  $d_{50}$  is the average particle size,  $Q$  is the particle loading,  $n_0$  is the refractive index of resin, and  $\Delta n$  is the refractive index difference between the particle and the resin. From this equation, curing depth can be decided by the particle size, the refractive index of the particle, and resin. In other words, use of particles having the high refractive index and small size in the composite decreases curing depth. Also, it has been reported that nanowires can enhance printing quality of the object by physical interaction with the resin [95,96]. The concentration of AgNW was decided as 1.9 vol % initially based on previous research in our research group [97,98], which demonstrated high conductivity. However, 3D printing process of DLP with 1.9 vol % (15.5 wt %) of AgNW was not successful, with numerous

defects in printed structures due to insufficiency of polymerization caused by light absorption of AgNWs. Therefore, the concentration of AgNW in resin was optimized as 13 wt % by considering the printability of DLP printer, which demonstrated well-defined structures in Figure 3.13(C), (D) by controlling sensitivity of the polymerization of the composite resin resulting from light absorption, scattering, and refractive properties of AgNWs while the resin without AgNWs in Figure 3.13(A), (B) showed over-cured and undefined structure in the core part.



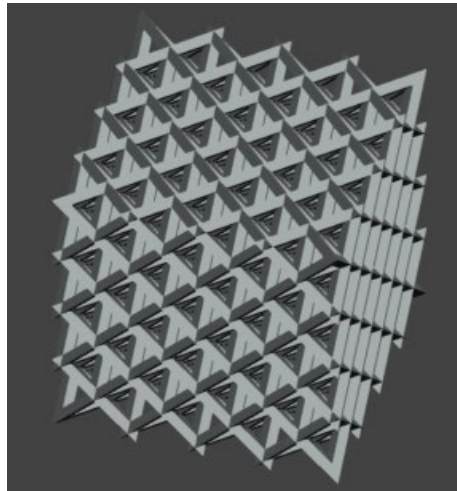
**Figure 3.13. Photographs of DLP printed octet with/without AgNWs (A), (B) without AgNWs, (C), (D) with AgNWs**

## **Chapter 4**

### **Design of 3D Electrode**




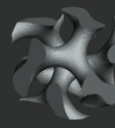
#### **4.1. Interdigitated electrode consisting of truss structure**

The electrodes are specifically designed using cellular structures, which allow the material to have superior mechanical properties at low weight and to have high specific surface area. One of the well-known stretching-dominant structures is the octet in Figure 4.1, whose elastic modulus and strength change linearly with relative density, making it stiffer than bending-dominated structures such as foam [99]. Many natural biological materials such as wood, bone, cork, plant stems, etc., demonstrate exceptional resilience and robustness which are drawn from their intricate mechanical network with many levels of hierarchy [100]. Even at smaller scales, it has been shown that introducing hierarchy into the architecture of 3D cellular structures. We can attain a unique combination of properties including low weight and linear scaling of strength and stiffness with density [101]. Therefore, adding hierarchy into the octet structures can be very advantageous for our experiment where we use pyrolysis to generate 3D electrodes. It is important to select mechanically durable structure because there is large stress applied during pyrolysis, resulting in structural collapse. Especially, as the printed electrodes are pyrolyzed in the presence of oxygen, decomposition of materials happens more vigorously, which causes collapse in the structure during pyrolysis.



**Figure 4.1. 3D model of octet structure 4x4x4 (total 64-unit cells)**

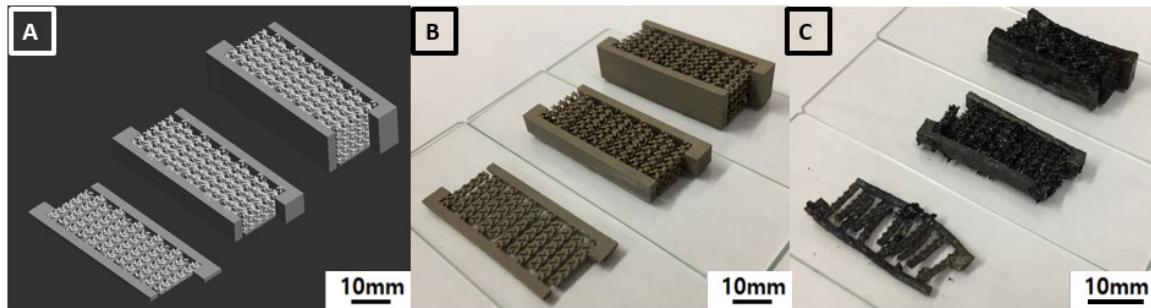
The specific surface area is an important element to increase performance of MSCs. By designing 3D electrode with octet structures, the specific surface area increases. Table 1 shows the surface area analysis of four different unit cell structures. The double gyroid structure, octet-thick (strut size:480  $\mu\text{m}$ ) and Octet-thin (strut size:300  $\mu\text{m}$ ) have five, six and nine times more specific surface area than that of solid.

				
	Solid	Octet-thick (480 $\mu\text{m}$ )	Octet-thin (300 $\mu\text{m}$ )	Double gyroid (480 $\mu\text{m}$ )
Vol (mm <sup>3</sup> )	13.82	3.32	1.85	2.52
Weight (g)	0.01686	0.00405	0.0022	0.003
Surface Area (mm <sup>2</sup> )	34.56- *5.76=28.8 *Basal plane	43.1	34.55	24.94
Specific Surface Area (mm <sup>2</sup> /g)	1708.2	10642	15287.6	8313.3

**Table 4.1. Surface area analysis of unit cell of electrode**

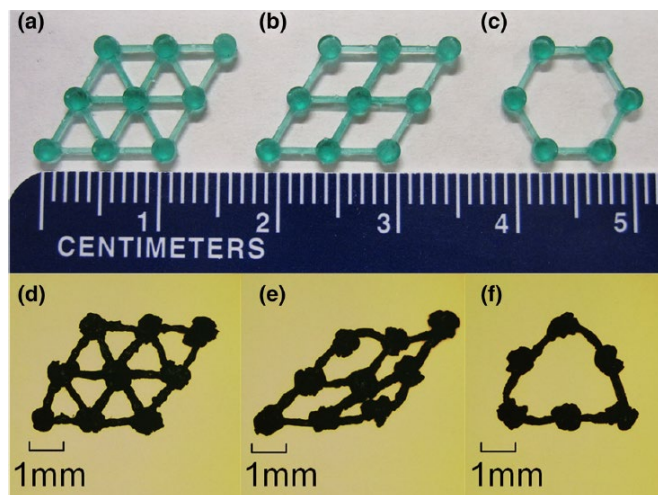
**(Solid vs Octet-thick vs Octet-thin vs Double gyroid)**

Initially, interdigitated electrodes consisting of double gyroid structures have been designed and printed to have high specific surface area as shown in Figure 4.2 A and B. However, the electrodes using double gyroid showed numerous defects, collapse and distortion in the structure after pyrolysis. (The pyrolysis process will be more explained in chapter 4.2.).



**Figure 4.2. (A): 3D modeling of IDE-double gyroid with different aspect ratio (3 mm, 6 mm, and 12 mm from left), (B): IDE-double gyroid as printed, (C): IDE-double gyroid after pyrolysis at 430 °C.**

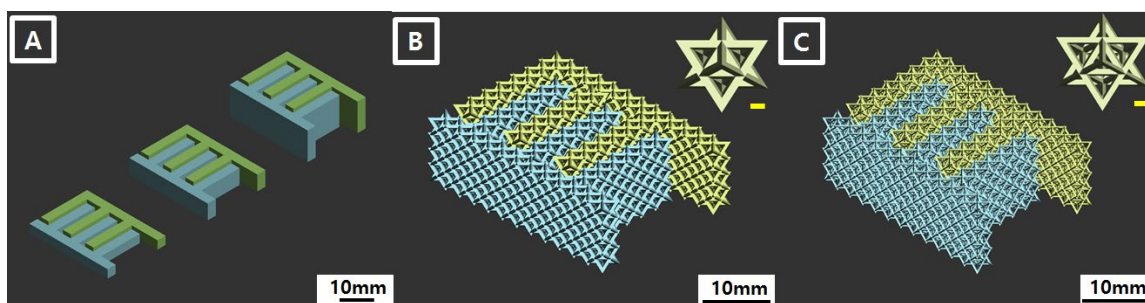
Another 3D architecture, *Octet*, has been selected by considering its higher relative elastic stiffness and shear modulus [99,102,103], which can resist plastic deformation of structure, contributing to maintaining rigid structure during pyrolysis [104]. The mechanical properties associated with the structural shapes have been reported [105].



**Figure 4.3. Comparison of different structures before and after pyrolysis; (a), (d): triangle, (b), (e): quadrangle, (e), (f): hexagon. Reprinted with permission [105].**

Figure 4.3 shows comparison of different structure before (a, b, c) and after (d, e, f) pyrolysis. This reveals that triangle shape (d) can maintain original shape after pyrolysis while the quadrangle (e) and hexagon (f) show large deformation or distortion after pyrolysis. This is because that the triangle supports have a significantly higher elastic stiffness and shear modulus than quadrangle and hexagon [105]. In these reasons, octet structure; rigid assemblies of octahedron and tetrahedron unit cells consisting of triangles could be an appropriate candidate for the 3D electrode to maintain the structure after pyrolysis.

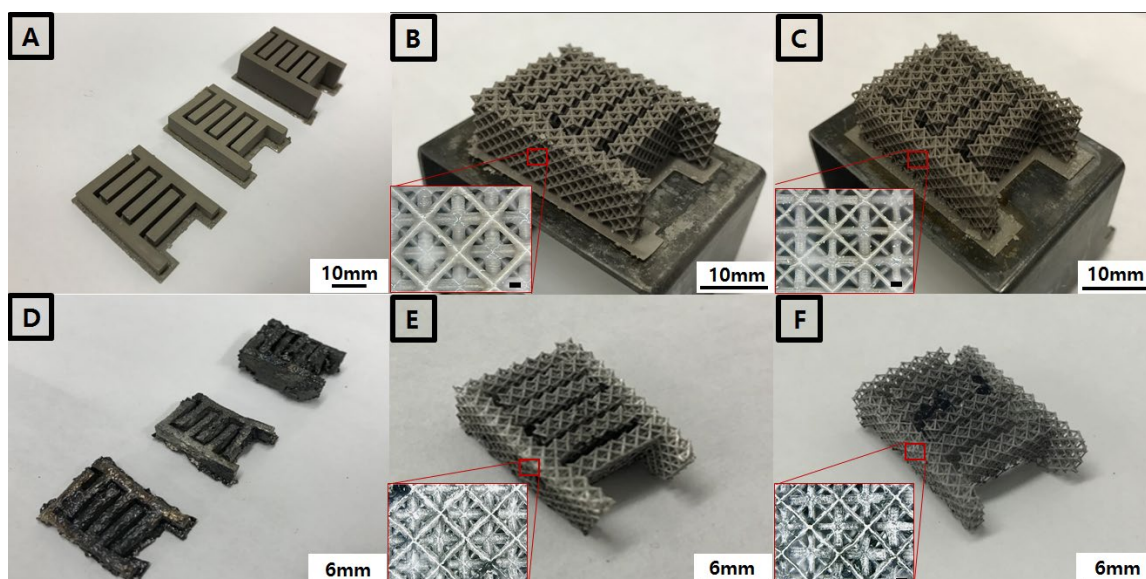
To study the durability of octet structures after pyrolysis, three structures were designed to have different surface areas: (1) solid, (2) octet-thick, and (3) octet-thin to fabricate MSCs, as shown in Figure 4.4(A–C). The total number of octet unit cell is 144 in both octet-thick and thick. The specific surface area (per gram) of each sample is: (1) Solid = 829 mm<sup>2</sup>/g, (2) octet-thick = 10642 mm<sup>2</sup>/g, (3) octet-thin = 15287.6 mm<sup>2</sup>/g based on computational 3D models. The specific surface area is only considered in electrode fingers.



**Figure 4.4. (A–C) 3D model images of interdigitated electrodes (IDEs). (A): IDE-solid with a different aspect ratio (3 mm, 6 mm, and 12 mm from left), (B): IDE-octet with thick (480 μm) strut size, (C): IDE-octet with thin (300 μm) strut size. (Inset: a unit cell of the octet, scale bar: 500 μm).**

By adding octet unit cells into IDE, instead of double gyroid, the structures can be survived without defects or collapses of the structure after pyrolysis 430 °C. Figure 4.5 illustrates photographs of the 3D printed IDEs before and after pyrolysis. It is observed that there are significant dimensional changes after pyrolysis: 40% size reduction and 88% weight loss. Interestingly, IDE-thick and IDE-thin remarkably showed light gray color, maintaining its structure even after pyrolysis in oxygen condition while the structure of IDE-solid collapsed partially and numerous cracks were observed. This structural stability of IDE-thick and IDE-thin after pyrolysis accounts for the superior mechanical properties of octet micro-trusses with

stretching-dominant behavior. Moreover, in case of the periodic cellular structure in IDE-thick and -thin, the flawless connectivity and continuity from 3D design and 3D printing allow the stress applied to be transferred and distributed to each unit cell during pyrolysis process.



**Figure 4.5. Photographs of 3D printed IDE based on 3D modeling as printed (A, B, C), after pyrolysis 430 °C (D, E, F). (Inset: digital microscope image of the printed electrode, scale bar: 500  $\mu\text{m}$ ).**

## 4.2. Pyrolysis of designed structure

The electrical resistance of printed IDEs was too high to be measured by a sourcemeter (resistance range  $<200\text{ M}\Omega$ ). Pyrolysis process, thermal heat treatment or decomposition of materials at elevated temperatures, was performed as a post treatment.

### 4.2.1. Experimental process

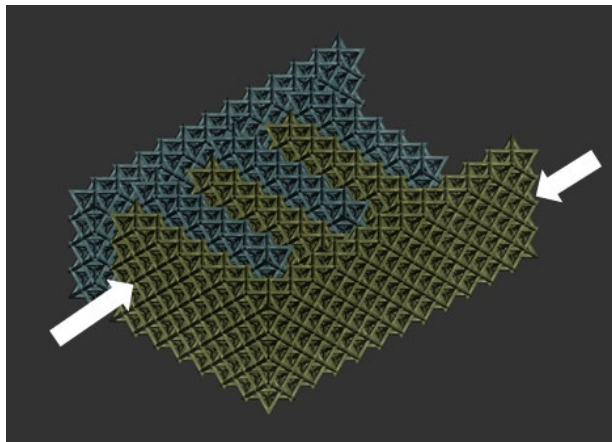
For the pyrolysis process of printed samples, pyrolysis temperature was decided based on reported thermogravimetric analysis (TGA) data of an acrylate polymer [106]. The TGA graph explains that there is significant weight reduction due to degradation of the polymer around 400–500 °C. We performed the pyrolysis experiment at 300°C, 375°C, 400 °C, 430 °C, 450 °C

and 500 °C for 30 min. Finally, the pyrolysis temperature for MSCs electrode was set at 430 °C by considering mechanical property and electrical resistance.

## 4.2.2. Characterization of pyrolyzed electrodes

### 4.2.2.1. Electrical resistance

Electrical resistance values of printed electrodes before and after pyrolysis were measured by a sourcemeter (Keithley 2400) with the two-wire DC resistance measurement method as shown in Figure 4.6. At 500 °C, the pyrolyzed structure even in IDE-octet showed significant structural collapses due to a large amount of decomposition. At 300 °C, the pyrolyzed IDE-octet did not show any significant defects such as structural distortion or collapse; however, the samples were nonconductive, with high resistance over 200 M $\Omega$ . The electrical resistances of IDE pyrolyzed at different temperatures are depicted in Figure 4.7. The resistance decreases as the pyrolysis temperature increase. The measured resistance of the IDE pyrolyzed at 450 °C was 13.8  $\Omega$ . (99.3 M $\Omega$  at 375 °C; 1.65 K $\Omega$  at 400 °; 40.176 $\Omega$  at 430 °C). It is required to optimize the pyrolysis temperature in terms of both conductivity and mechanical property. As temperature increases, the conductivity can be enhanced. However, at the same time, the mechanical properties of IDE are degraded by the decomposition of the polymer parts. Therefore, the furnace temperature was optimized as 430 °C for 30 min for the MSCs application by considering high electrical conductivity and mechanical sustainability of 3D structures.



**Figure 4.6. Contact points for electrical resistance measurement**



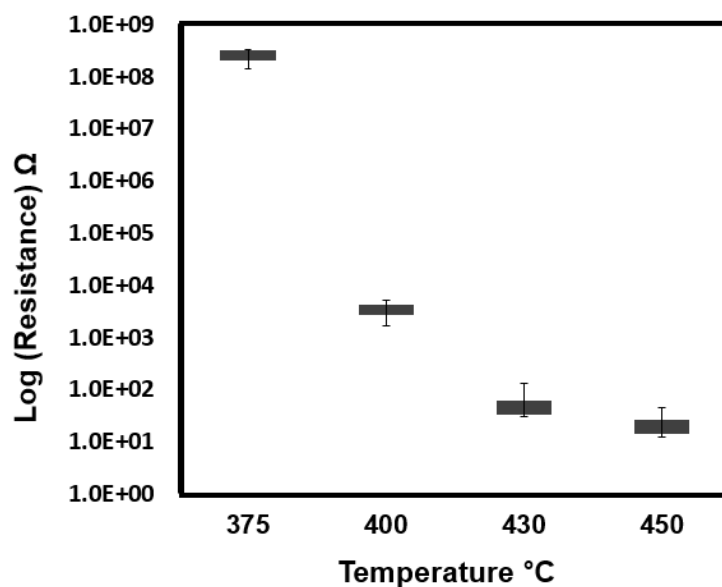
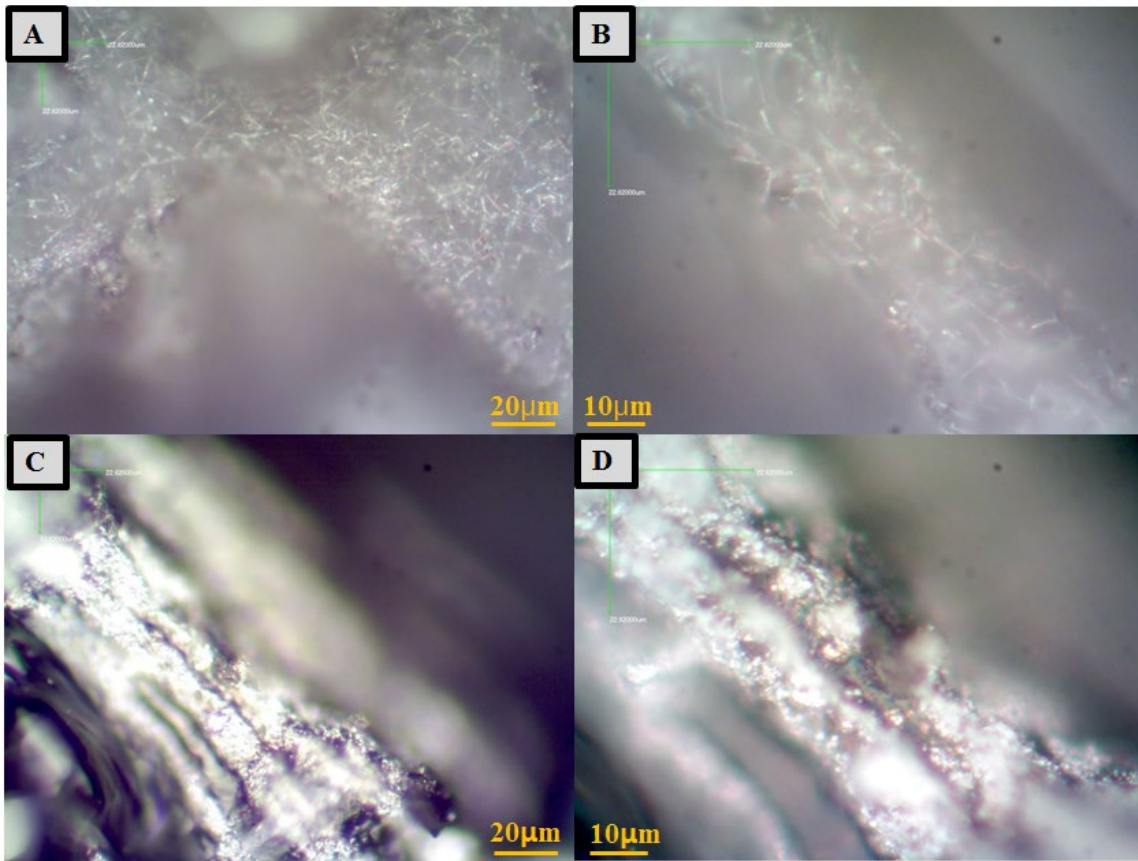


Figure 4.7. Plot of the resistances with respect to different pyrolysis temperature

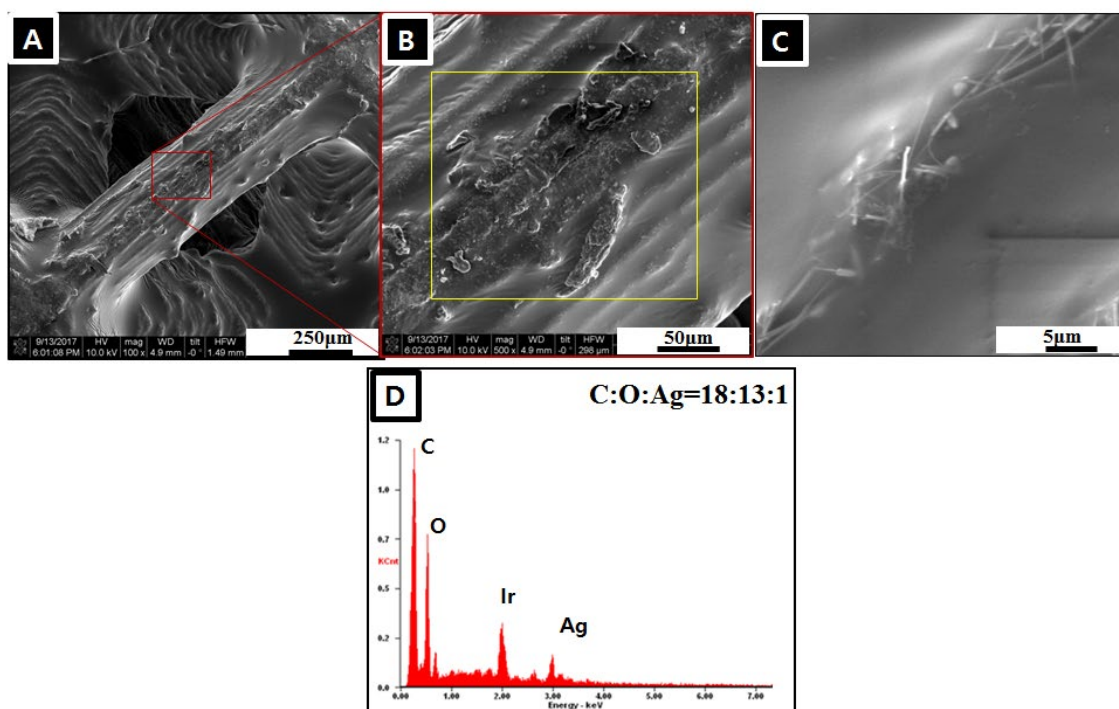
#### 4.2.2.2. Morphology & Composition analysis

To characterize the morphology of printed electrodes, digital optical microscopy and scanning electron microscopy (SEM) analysis were carried out. Also, energy-dispersive X-ray spectroscopy (EDS) analysis was performed to see the relative composition of 3D printed electrodes before and after pyrolysis.



**Figure 4.8. Optical microscopy images with difference magnification: IDE as printed in (A) and (B); IDE after pyrolysis in (C), and (D)**

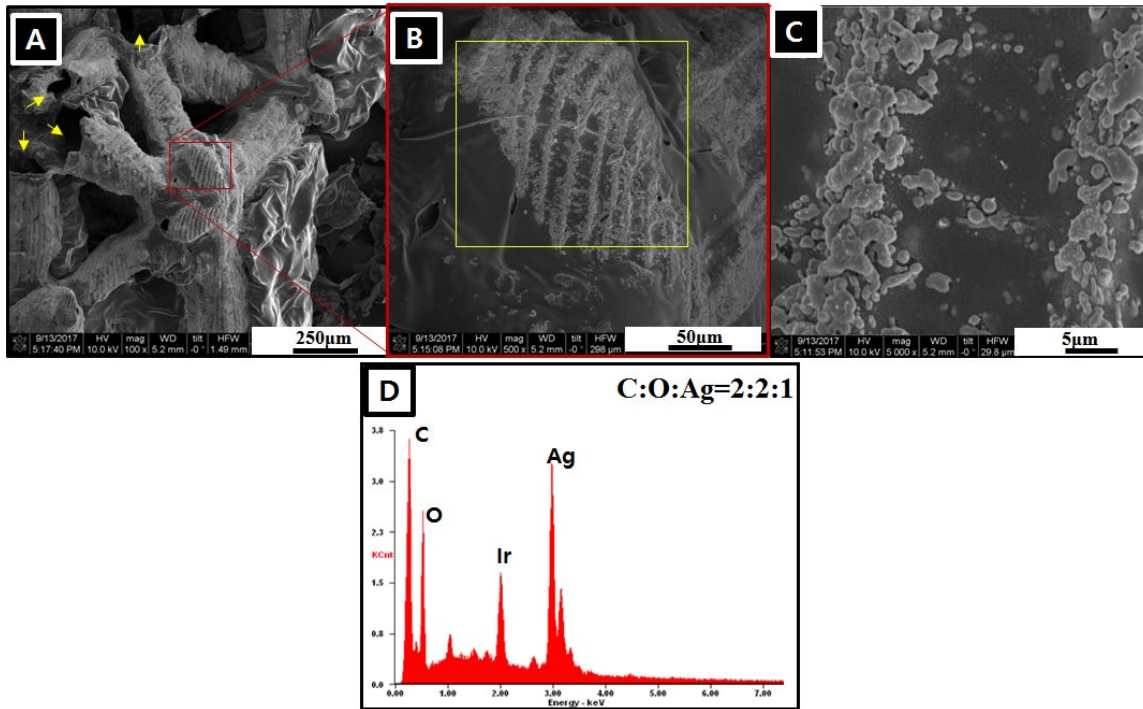
Figure 4.8 depicts the morphology of printed IDE before & after pyrolysis at different magnification by optical microscopy. In the Figure 4.8(A), (B), before pyrolysis, numerous AgNWs are observed. However, after pyrolysis in the Figure 4.8(C), (D), the AgNWs are not observed anymore. Instead, coalescence of the brighter color can be seen. The SEM & EDS analysis explain these phenomena with the magnified images and the composition of the IDE. Figure 4.9(A-C) represents SEM images of IDE as printed at different magnification.



**Figure 4.9. Scanning electron microscope images of 3D printed IDE. (A–C) As printed. (D) EDS spectra of IDE as printed in the selected yellow area of (B)**

IDE-thin (as printed) illustrates layer by layer laminar structures indicating typical DLP printing stacking patterns corresponding to the layer thickness of resolution information (30  $\mu\text{m}$ ) shown in Figure 4.9(A), (B). SEM images of IDE-thin after pyrolysis in Figure 4.10(A), (B) clearly show hollow structure as noted by yellow arrows and more bright color patterns on the surface of the structure corresponding to silver, based on the EDS profile in Figure 4.10(D) in the profiles of the yellow square region of Figure 4.10(B). This can be more explained by EDS in Figure 4.10(D) where it shows higher silver atomic weight while Figure 4.9(D) shows lower silver atomic weight. In detail, the atomic weight ratio of carbon: silver before and after pyrolysis indicates significant atomic weight (at %) change from 18:1 to 2:1, which would be the main cause of high electrical conductivity of IDE-octet after pyrolysis. Measured resistance was 1.65 K $\Omega$  in IDC-thick with standard deviation of 59.91. Also, IDC-thin showed resistance values of 40.2  $\Omega$  with standard deviation of 35.4 on average. Higher resistance of IDC-thick results from insufficient decomposition of the polymer inside and less sintering of silver to produce interconnected conductive structures. The highly concentrated silver network in IDE-thin is mainly attributed to more decomposition of acrylate units in the polymeric parts. The sintering of

AgNWs generates silver-interconnected 3D structure, maintaining its structure with help from the octet structure.



**Figure 4.10. Scanning electron microscope images of 3D printed IDE (A–C) after pyrolysis. (D) EDS spectra of and IDE after pyrolysis in the selected yellow area of (B).**

This can be observed in Figure 4.9(C) more clearly where the AgNWs are embedded in photo-cured resin in accordance with the layer pattern of 3D printing, while the morphology of AgNWs is changed after pyrolysis in Figure 4.10(C) and eventually spheroidized [107]. The mechanism of instable morphology in AgNWs originates from Rayleigh or Plateau– Rayleigh instability [108,109] where atomic diffusion is enhanced as temperature is increased. At higher temperature such as 430 °C, AgNWs tend to lower their surface energy by assuming a spherical shape. The spheroidized AgNWs come closely each other by the decomposition of polymeric parts. Then, the spheroidized AgNWs are sintered to generate 3D network structures. Additionally, the hollow structures can be related to the catalyst reaction of silver, increasing the gas yield and reducing the charcoal yield [110]. Therefore, the acrylate starts to decompose in the center of the strut, making voids, and those voids emerge in the centers. AgNWs migrate into the outer shell, and those are aggregated and sintered, making an interconnected silver.

Figure 4.11 explains that the brighter patterns are sintered silver based on EDS analysis. EDS spectra (B) from selected region in (A), dark region, shows lower peak of Ag where the atomic weight ratio between C: Ag is 39:15. EDS spectra (D) from selected region in (C), bright region, shows higher peak of Ag where the ratio of C: Ag is 13:69.

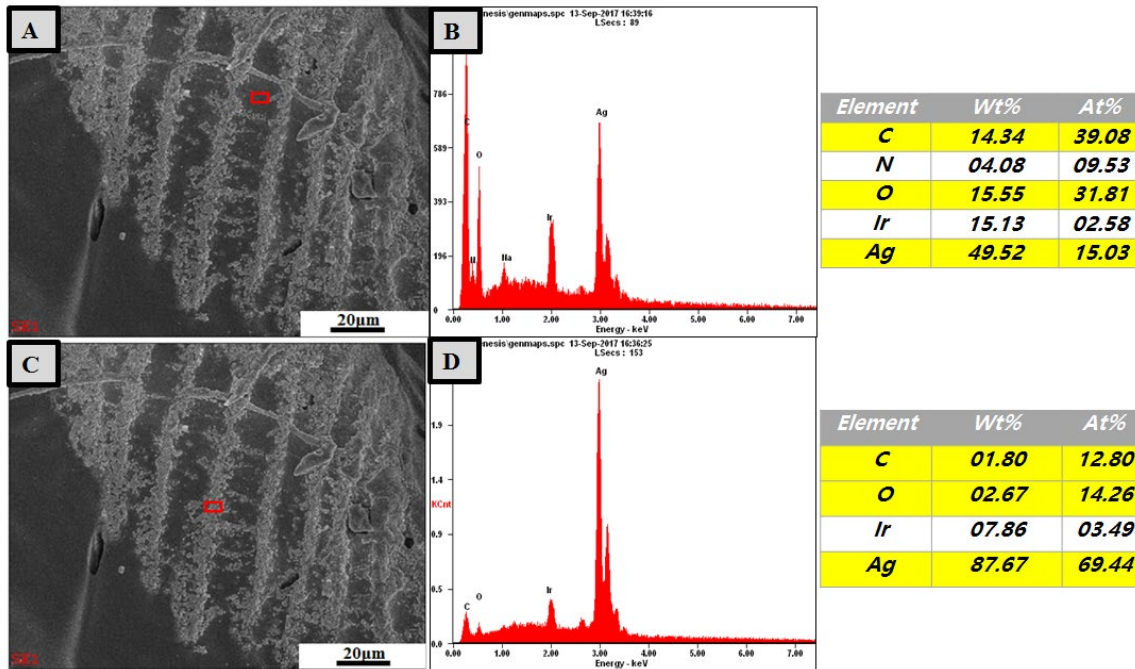


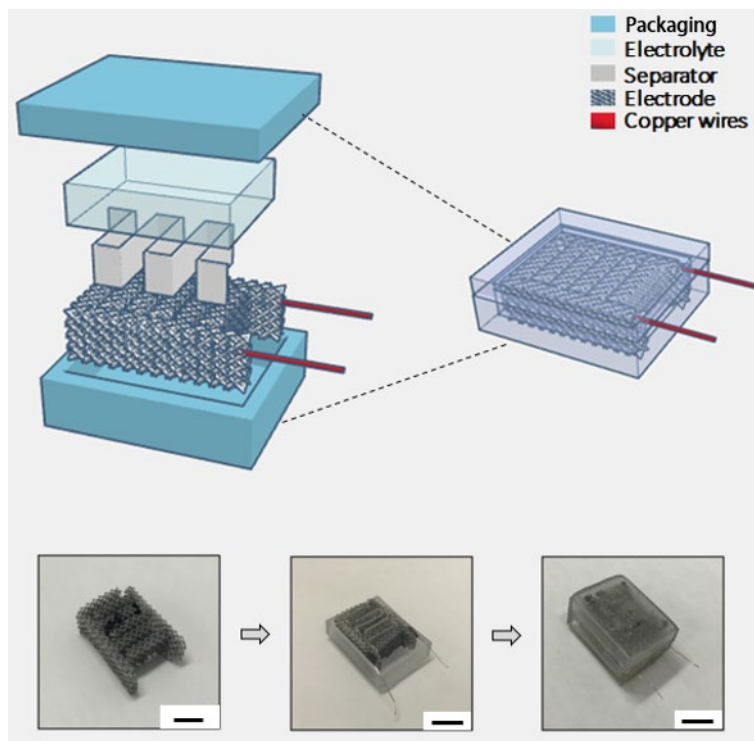
Figure 4.11. EDS spectra in char (A, B) and in silver (C, D) after pyrolysis.

## Chapter 5

### 3D printed micro-supercapacitor

#### 5.1. Fabrication process

The IDE MSCs devices (IDC) were fabricated as depicted in Figure 5.1. The gel-type electrolyte was prepared using PVA (1 g),  $\text{LiClO}_4$  (0.34 g) and deionized water (10 mL). The solid PVA and  $\text{LiClO}_4$  were dissolved in deionized water (10 mL) and heated to 90 °C with vigorous stirring for 24 h. MSCs cases were also printed by the DLP printer for packaging. Filter paper, Whatman 1001-150, was used as a separator to prevent a possible electrical short between the two electrodes caused by capillary force of PVA and the silver electrodes [111]. Finally, copper wires were connected to each electrode with carbon glue to create electrical contacts for electrochemical characterization. Fabricated MSCs were dried in ambient air conditions and stabilized for 24 hrs to make electrolyte fully diffuse in the electrodes.

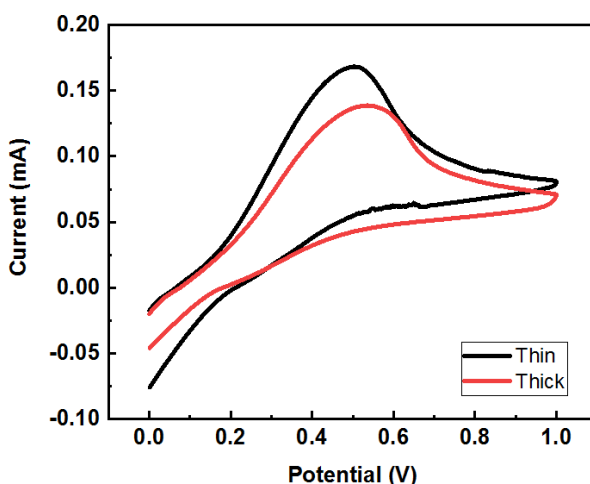


**Figure 5.1. Schematics of fabrication process of MSCs(Upper) Photographs of fabrication process (Lower), scale bar:10 mm**

## 5.2 Performance evaluation of micro-supercapacitor

### 5.2.1. Cyclic Voltammeter

Cyclic voltammetry (CV) test was performed to evaluate electrochemical characteristics with an electrochemical analyzer (CHI 1205B, CH Instruments, Inc.). Two electrodes set-up was applied to analyze the total cell performance in the MSCs where counter electrode (CE) and reference electrode (RE) are both connected to one electrode while working electrode (WE) is connected to the other electrode. By using two electrodes system, the potential difference over the entire cell is measured. This is useful when the whole cell's performance is interesting by considering combination of working electrode, the electrolytes resistance, ohmic resistance and counter/reference electrode.



**Figure 5.2. Cyclic voltammetry curve; black is octet-thin and red is octet- thick**

In this CV test, the current is measured as a function of voltage. Minimum and maximum voltage is set 0 to 1V and different scan rate (mV/s) can be applied. The result of CV can be obtained as plots on the graph: current on y axis and voltage on the x axis. The potential difference between the working electrode and reference is recorded. The capacitance of the MSCs was calculated from CV data using equation (eq4) as below:

$$C_{cell} = \frac{\int i(V)dV}{2Vv} \quad (4)$$

where  $i$  is the current,  $V$  is the voltage, and  $v$  is the scan rate. CV test results, measured by a two-electrode system, are shown in Figure 5.2 and depict the performance of two (IDC-thin and IDC-thick) different devices at 200 mV/s scan rate in 0 to 1 voltage ranges. The specific capacitance of IDC-thin is 3.01 mF/g (0.301 mF/cm<sup>2</sup>) while that of IDC-thick is 1.41 mF/g (0.206 mF/cm<sup>2</sup>). This can be explained by the higher specific surface area of IDC-thin, as it is designed, and the higher conductivity [112] of IDC-thin than that of IDC-thick, contributing to higher capacitance. Both graphs exhibit sigmoidal behavior resulting from the silver redox reaction [113,114]. The energy storage of MSCs can be explained by two possible mechanisms: First, electrostatic double layer capacitance (EDLC) can be generated on the IDC electrodes by electrostatic accumulation of surface charge. Because the capacitance of EDLC highly depends on the surface area of the electrode, hierarchically designed 3D electrodes having the higher surface area can increase the capacitance. However, the CV curve in Figure 5.2 indicates that both graphs are not pseudo rectangular. This indicates that the generated capacitance from EDLC will be minor. Therefore, the predominant energy storage of 3D printed MSCs is mainly attributed to redox reactions in the silver 3D structure:  $Ag_0 \leftrightarrow Ag^+ + e^-$ ,  $2Ag^+ + 2OH^- \rightarrow Ag_2O + H_2O$  [113,114]. This pseudocapacitive behavior can increase total capacitance of MSC coupled with EDLC by overcoming the relatively low specific capacitance of EDLC.



## 5.2.2. Galvanostatic charge/discharge

Galvano charge/discharge (GCD) was conducted by CT2001a battery tester (Landt Instruments)

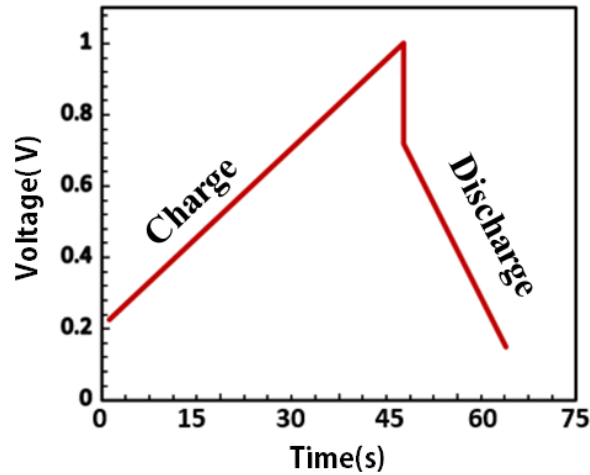


Figure 5.3. Galvanostatic charge/discharge curve of IDE-Thin at 0.2 mA.

Galvanostatic charge/discharge (GCD) curve of IDC-thin supercapacitor at a constant current of 0.2 mA is shown in Figure 5.3. Nearly linear charge/discharge profiles were obtained as an indication of good capacitor behavior. However, there was a large IR drop at the beginning of the discharge curve attributed to the internal resistance, i.e., electrode resistance, interfacial resistance and electrolyte ionic resistance [115–117]. The cell capacitances from the GCD curve was calculated by using following equation (eq5):

$$C_{Cell} = \frac{i\Delta t}{\Delta V} \quad (5)$$

where  $i$  is the current,  $V$  is the voltage, and  $t$  is the discharge time in seconds. The areal capacitance is 1.33 mF/cm<sup>2</sup> based on the calculation.

# Chapter 6

## Conclusion and Future Work

### 6.1. Conclusion

In this thesis, a photo-curable conductive resin for DLP 3D printing has been developed. 3D printing followed by pyrolysis of photo-cured silver/acrylate demonstrated low electrical resistance. Then, 3D electrodes having mechanically durable truss, and high surface area were printed. Finally, the developed 3D electrodes were assembled with the electrolyte to demonstrate 3D micro-supercapacitor. The main achievement of this thesis is like below.

1. Design and optimization of photo-curable conductive resin for digital light processing 3D printer;

A photo-curable conductive resin consisting of the monomer (35wt%), oligomer (65wt%), photo- initiator (3wt% of resin) and AgNWs (13wt% of resin) were formulated by considering photo-curing mechanism, viscosity and light absorption effect. The printability was demonstrated by printing a highly complex structure.

2. Characterization of 3D printed electrode after pyrolysis;

The 3D printed electrode after pyrolysis shows unique silver morphology corresponding to 3D printing layers. The electrical resistance of 40.2  $\Omega$  was achieved at the pyrolysis temperature of 430 °C. The decomposition of the polymer and sintering of silver are the main mechanism of high conductive structure.

3. 3D electrode design;

As a main advantage of 3D printing, tailored design of electrodes is possible. The interdigitated electrodes consisting of mechanically durable 3D complex truss structures were designed and printed successfully. The truss design contributes to durable property while it is pyrolyzed, resulting in maintaining its structures.

4. Fabrication of micro-supercapacitor and demonstration of performance;  
3D electrodes with gel-type electrolyte were fabricated and the areal capacitance of 0.301 mF/cm<sup>2</sup> was achieved.

The demonstrated approach can be utilized for next-generation 3D electrode designs by 3D printing for the following reasons: 1) The interconnected silver materials offer a 3D continuous electron pathway and the ordered pores allow the electrolyte to penetrate and diffuse evenly between electrodes. 2) Freestanding electrodes without current collector are capable with 3D printed electrodes, offering facile and low-cost fabrication. 3) It has freedom of geometrical design in specific application with scale up environments. 4) It is achievable to reduce size of electrode structure by high resolution DLP printer and pyrolysis method, generating hierarchical macroporous framework which can have high surface area and ideal size for electrolyte diffusion and its electrochemical performance can be significantly enhanced by deposition of electrochemical active materials.

## 6.2. Future Works

1. To improve electro-chemical performance in MSCs, deposition of pseudo active materials on the 3D printed electrode is a promising approach.
2. To have superior mechanical property, pyrolysis process with inert gas such as H<sub>2</sub>, N<sub>2</sub> at higher temperature can be performed. Finally, polymer material selection or additives can be more carefully designed for better carbon yield.

## Reference

1. M. Winter, R. J. Brodd, "What Are Batteries, Fuel Cells, and Supercapacitors?" *Chemical Reviews*, vol. 104, p.4245–4270, 2004.
2. P. Simon, Y. Gogotsi, "Materials for electrochemical capacitors" *Nat. Mater.*, vol. 7, p. 845–854, 2008.
3. T. Brezesinski, J. Wang, S. H. Tolbert, B. Dunn, "Ordered mesoporous  $\alpha$ -MoO<sub>3</sub> with iso-oriented nanocrystalline walls for thin film pseudocapacitors" *Nat. Mater.* Vol. 9, p.146–151, 2010.
4. L. L. Zhang, X.S. Zhao, "Carbon-based materials as supercapacitor electrodes". *Chem. Soc. Rev.* vol. 38, p.2520–2531, 2009.
5. W. Sun, G. Gao, Y. Du, K. Zhang, G Wu, "A Facile Strategy for Fabricating Hierarchical Nanocomposites of V<sub>2</sub>O<sub>5</sub> Nanowire Arrays on a Three-Dimensional N-Doped Graphene Aerogel with a Synergistic Effect for Supercapacitors" *J. Mater. Chem. A.* vol. 6, p.9938–9947, 2018.
6. N. A. Kyeremateng, T. Brousse, D. Pech, "Microsupercapacitors as miniaturized energy-storage components for on-chip electronics". *Nat. Nanotechnol.* 2017, 12, 7–15.
7. W. Sun, R. Zheng, X. Chen, "Symmetric redox supercapacitor based on micro-fabrication with three-dimensional polypyrrole electrodes" *J. Power Sources.* vol. 195, p.7120–7125, 2010.
8. M. Beidaghi, C. Wang, "Micro-supercapacitors based on three dimensional interdigital polypyrrole/C-MEMS electrodes" *Electrochim. Acta.* vol. 56, p.9508–9514, 2011.
9. V. Malgras, Q. Ji, Y. Kamachi, T. Mori, F.K. Shieh, K.C. Wu, K. Ariga, Y. Yamauchi, "Templated synthesis for nanoarchitected porous materials". *Bull. Chem. Soc. Jpn.* vol. 88, p.1171–1200, 2015.
10. K. Sun, T. S. Wei, B. Y. Ahn, J. Y. Seo, S. J. Dillon, J. A. Lewis, "3D printing of interdigitated Li-ion microbattery architectures". *Adv. Mater.* Vol.25, p.4539–4543, 2013.
11. W. Li, Y. Li, M. Su, B. An, J. Liu, D. Su, L. Li, F. Li, Y. Song, "Printing assembly and structural regulation of graphene towards three-dimensional flexible micro-supercapacitors". *J. Mater. Chem. A* vol. 5, p.16281–16288, 2017.
12. C. Zhao, C. Y. Wang, R. Gorkin, S. Beirne, K. W. Shu, G. G. Wallace, "Three

- dimensional (3D) printed electrodes for interdigitated supercapacitors”. *Electrochem. Commun.* vol. 41, p.20–23, 2014.
13. C. W. Foster, M. P. Down, Y. Zhang, X. Ji, S. J. Rowley-Neale, G. C. Smith; P. J. Kelly, C. E. Banks, “3D printed graphene-based energy storage devices”. *Sci. Rep.* vol. 7, p.42233, 2017.
  14. X. Zheng, J. Deotte, M. P. Alonso, G. R. Farquar, T. H. Weisgraber, S. Gemberling, H. Lee, N. Fang, C. M. Spadaccini, “Design and optimization of a light-emitting diode projection micro-stereolithography three-dimensional manufacturing system”. *Rev. Sci. Instrum.* vol. 83, 125001. 2012.
  15. X. Y. Zheng, H. Lee, T. H. Weisgraber, M. Shusteff, J. DeOtte, E. B. Duoss, J. D. Kuntz, M. M. Biener, Q. Ge, J. A. Jackson, S. O. Kucheyev, N. X. Fang, C. M. Spadaccini, “Ultralight, ultrastiff mechanical metamaterials”. *Science.* vol. 344, p.1373–1377, 2014.
  16. N. W. Bartlett, M. T. Tolley, J. T. B. Overvelde, J. C. Weaver, B. Mosadegh, K. Bertoldi, G. M. Whitesides, R. J. A. Wood, “3Dprinted, functionally graded soft robot powered by combustion” *Science.* vol. 349, p.161–165, 2015.
  17. E. Fantino, A. Chiappone, I. Roppolo, D. Manfredi, R. Bongiovanni, C. F. Pirri, F. Calignano, “3D Printing of Conductive Complex Structures with In Situ Generation of Silver Nanoparticles”. *Adv. Mater.* vol. 28, p3712–3717, 2016.
  18. Q. Mu, L. Wang, C. K. Dunn, X. Kuang, F. Duan, Z. Zhang, H. J. Qi, T. Wang, “Digital light processing 3D printing of conductive complex structures”. *Addit. Manuf.* Vol. 18, p74–83, 2017
  19. G. Gonzalez, A. Chiappone, I. Roppolo, E. Fantino, V. Bertana, F. Perrucci, L. Scaltrito, F. Pirri, M. Sangermano, “Development of 3D printable formulations containing CNT with enhanced electrical properties”. *Polymer.* vol.109, 246–253, 2017.
  20. J. W. Long, D. B´elanger, T. Brousse, W. Sugimoto, M. B. Sassin and O. Crosnier, *MRS Bull.* vol. 36, p.513–522. 2011.
  21. L.L. Zhang, X.S. Zhao, “Carbon-based materials as supercapacitor electrodes”, *Chem. Soc. Rev.* vol. 38, p.2520–2531, 2009.
  22. C. Liu, Z. Yu, D. Neff, A. Zhamu, B.Z. Jang, “Graphene-Based Supercapacitor with an Ultrahigh Energy Density”, *Nano Letters.* vol. 10, 4863–4868. 2010.
  23. A. Ferris, S. Garbarino, D. Guay, D. Pech, “3D RuO<sub>2</sub>Microsupercapacitors with Remarkable Areal Energy”, *Advanced Materials.* vol. 27, p.6625–6629, 2015.

24. G. Yu, L. Hu, N. Liu, H. Wang, M. Vosgueritchian, Y. Yang, Y. Cui, Z. Bao, "Enhancing the Supercapacitor Performance of Graphene/MnO<sub>2</sub> Nanostructured Electrodes by Conductive Wrapping", *Nano Letters*. vol. 11, p.4438–4442, 2011.
25. F. Su, X. Lv, M. Miao, "High-Performance Two-Ply Yarn Supercapacitors Based on Carbon Nanotube Yarns Dotted with Co<sub>3</sub>O<sub>4</sub> and NiO Nanoparticles", *Small*. vol. 11 p.854–861, 2014.
26. Q. Liao, N. Li, S. Jin, G. Yang, C. Wang, "All-Solid-State Symmetric Supercapacitor Based on Co<sub>3</sub>O<sub>4</sub> Nanoparticles on Vertically Aligned Graphene", *ACS Nano*. 9 p.5310–5317, 2015.
27. L. Li, Z. Lou, W. Han, D. Chen, K. Jiang, G. Shen, "Highly Stretchable Micro-Supercapacitor Arrays with Hybrid Mwcnt/Pani Electrode". *Adv. Mater. Technol.* vol. 2, p. 1600282, 2017.
28. K. Naoi, S. Ishimoto, N. Ogihara, Y. Nakagawa, S. Hatta, *J. Electrochem. Soc.* Vol. 156 A52 2009.
29. W. Lv, D. K. Tang, D. Y.B. He, C. H. You, Z. Q. Shi, X. C. Chen, C. M Chen, P. X. Hou, C. Liu, Q. H. Yang, *ACS Nano*. vol. 3, p.3730–3736, 2009.
30. S. Peng, L. Li, H. Tan, R. Cai, W. Shi, C. Li, et al., "Hollow Spheres: MS<sub>2</sub> (M = Co and Ni) Hollow Spheres with Tunable Interiors for High-Performance Supercapacitors and Photovoltaics" *Advanced Functional Materials*. vol. 24 p.2154–2154, 2014.
31. Z. Chen, V. Augustyn, J. Wen, Y. Zhang, M. Shen, B. Dunn, Y. Lu, "High-Performance Supercapacitors Based on Intertwined CNT/V<sub>2</sub>O<sub>5</sub> Nanowire Nanocomposites", *Advanced Materials*. vol. 23, p.791–795, 2011.
32. K.H. An, W.S. Kim, Y.S. Park, J.-M. Moon, D.J. Bae, S.C. Lim, et al., "Electrochemical Properties of High-Power Supercapacitors Using Single-Walled Carbon Nanotube Electrodes", *Advanced Functional Materials*. vol. 11, p. 387–392. 2001.
33. R.B. Rakhi, W. Chen, M.N. Hedhili, D. Cha, H.N. Alshareef, "Enhanced Rate Performance of Mesoporous Co<sub>3</sub>O<sub>4</sub> Nanosheet Supercapacitor Electrodes by Hydrous RuO<sub>2</sub> Nanoparticle Decoration", *ACS Applied Materials & Interfaces*. Vol. 6, p.4196–4206, 2014.
34. S.I. Kim, J.S. Lee, H.J. Ahn, H.K. Song, J.H. Jang, "Facile Route to an Efficient NiO Supercapacitor with a Three-Dimensional Nanonetwork Morphology", *ACS Applied Materials & Interfaces*. vol. 5, p.596–1603. 2013.
35. Y.J. Kim, Y.A. Kim, T. Chino, H. Suezaki, M. Endo, M.S. Dresselhaus, "Chemically

- Modified Multiwalled Carbon Nanotubes as an Additive for Supercapacitors”, *Small*. vol. 2, p. 339–345, 2006.
36. R. Yuksel, S. Coskun, H.E. Unalan, “Coaxial silver nanowire network core molybdenum oxide shell supercapacitor electrodes”, *Electrochimica Acta*. vol. 193, p.39–44. 2016.
  37. J. Chen, H. Bi, S. Sun, Y. Tang, W. Zhao, T. Lin, et al., “Highly Conductive and Flexible Paper of 1D Silver-Nanowire-Doped Graphene”, *ACS Applied Materials & Interfaces*. vol. 5, p.1408–1413.2013.
  38. X. Dong, C.-Y. Su, W. Zhang, J. Zhao, Q. Ling, W. Huang, et al., “Ultra-large single-layer graphene obtained from solution chemical reduction and its electrical properties”, *Physical Chemistry Chemical Physics*. vol. 12, p.2164, 2010.
  39. X. Yang, J. Zhu, L. Qiu, D. Li, “Bioinspired Effective Prevention of Restacking in Multilayered Graphene Films: Towards the Next Generation of High-Performance Supercapacitors”, *Advanced Materials*. vol. 23 p. 2833–2838, 2011.
  40. L. Zhang, F. Zhang, X. Yang, G. Long, Y. Wu, T. Zhang, et al., “Porous 3D graphene-based bulk materials with exceptional high surface area and excellent conductivity for supercapacitors”, *Scientific Reports*. vol. 3, 2013.
  41. U.N. Maiti, J. Lim, K.E. Lee, W.J. Lee, S.O. Kim, Gelation, “Three-Dimensional Shape Engineered, Interfacial Gelation of Reduced Graphene Oxide for High Rate, Large Capacity Supercapacitors”, *Adv. Mater.* vol. 26, p.505–505, 2014.
  42. Y. Yoon, K. Lee, C. Baik, H. Yoo, M. Min, Y. Park, et al., “Anti-Solvent Derived Non-Stacked Reduced Graphene Oxide for High Performance Supercapacitors”, *Advanced Materials*. vol. 25, p.4437–4444, 2013.
  43. X.C. Dong, H. Xu, X.W. Wang, Y.X. Huang, M.B. Chan-Park, H. Zhang, L.H Wang, W. Huang, P. Chen. “3D Graphene–Cobalt Oxide Electrode for High-Performance Supercapacitor and Enzymeless Glucose Detection”, *ACS Nano*. vol. 6, p.3206–3213, 2012.
  44. X. Cao, Y. Shi, W. Shi, G. Lu, X. Huang, Q. Yan, et al., “Preparation of Novel 3D Graphene Networks for Supercapacitor Applications”, *Small*. vol. 7, p.3163–3168, 2011.
  45. M.F. El-Kady, V. Strong, S. Dubin, R.B. Kaner, “Laser Scribing of High-Performance and Flexible Graphene-Based Electrochemical Capacitors”, *Science*. vol. 335 p.326–1330, 2012.

46. M.F. El-Kady, R.B. Kaner, “Scalable fabrication of high-power graphene micro-supercapacitors for flexible and on-chip energy storage”, *Nature Communications*. Vol. 4, 2013.
47. J. Cai, C. Lv, A. Watanabe, “Cost-effective fabrication of high-performance flexible all-solid-state carbon micro-supercapacitors by blue-violet laser direct writing and further surface treatment”, *Journal of Materials Chemistry A*. vol. 4, p.1671–1679, 2016.
48. J. Lee, J.Y. Seok, S. Son, M. Yang, B. Kang, “High-energy, flexible micro-supercapacitors by one-step laser fabrication of a self-generated nanoporous metal/oxide electrode”, *Journal of Materials Chemistry A*. vol. 5. p.24585–24593, 2017.
49. P. Chen, H. Chen, J. Qiu, C. Zhou, “Inkjet printing of single-walled carbon nanotube/RuO<sub>2</sub> nanowire supercapacitors on cloth fabrics and flexible substrates”, *Nano Research*. vol. 3, p.594–603, 2010.
50. L.T. Le, M.H. Ervin, H. Qiu, B.E. Fuchs, W.Y. Lee, “Graphene supercapacitor electrodes fabricated by inkjet printing and thermal reduction of graphene oxide”, *Electrochemistry Communications*. vol. 13, p. 355–358, 2011.
51. J. Li, F. Ye, S. Vaziri, M. Muhammed, M.C. Lemme, M. Östling, “Efficient Inkjet Printing of Graphene”, *Advanced Materials*. vol. 25, p.3985–3992, 2013.
52. K. H. Choi, J. Yoo, C.K. Lee, S.Y. Lee, “All-inkjet-printed, solid-state flexible supercapacitors on paper”, *Energy & Environmental Science*. vol. 9 p.2812–2821, 2016.
53. W. Li, Y. Li, M. Su, B. An, J. Liu, D. Su, et al., “Printing assembly and structural regulation of graphene towards three-dimensional flexible micro-supercapacitors”, *Journal of Materials Chemistry A*. vol. 5, p.16281–16288, 2017.
54. W. Yu, H. Zhou, B.Q. Li, S. Ding, “3D Printing of Carbon Nanotubes-Based Microsupercapacitors”, *ACS Applied Materials & Interfaces*. vol. 9, p.4597–4604, 2017.
55. B. Chen, Y. Jiang, X. Tang, Y. Pan, S. Hu, “Fully Packaged Carbon Nanotube Supercapacitors by Direct Ink Writing on Flexible Substrates”, *ACS Appl. Mater. Interfaces*. vol. 9, p.28433-28440, 2017.
56. Z. Wang, Q. Zhang, S. Long, Y. Luo, P. Yu, Z. Tan, J. Bai, B. Qu, Y. Yang, J. Shi, H. Zhou, Z.Y. Xiao, W. Hong, H. Bai, “Three-Dimensional Printing of Polyaniline/Reduced Graphene Oxide Composite for High-Performance Planar Supercapacitor”, *ACS Applied Materials & Interfaces*. vol. 10, p.10444, 2018.
57. K. Shen, J. Ding, S. Yang, “3D Printing Quasi-Solid-State Asymmetric Micro-



- Supercapacitors with Ultrahigh Areal Energy Density, *Advanced Energy Materials*. vol. 8, p.1800408, 2018.
58. A. Mahajan, C.D. Frisbie, L.F. Francis, "Optimization of Aerosol Jet Printing for High-Resolution, High-Aspect Ratio Silver Lines", *ACS Applied Materials & Interfaces*. vol. 5 p.4856–4864, 2013.
  59. J.A. Paulsen, M. Renn, K. Christenson, R. Plourde, "Printing conformal electronics on 3D structures with Aerosol Jet technology", 2012 Future of Instrumentation International Workshop (FIIW) Proceedings, 2012.
  60. M.S. Saleh, C. Hu, R. Panat, "Three-dimensional microarchitected materials and devices using nanoparticle assembly by pointwise spatial printing", *Science Advances*. vol. 3, 2017.
  61. M.S. Saleh, J. Li, J. Park, R. Panat, "3D printed hierarchically-porous microlattice electrode materials for exceptionally high specific capacity and areal capacity lithium on batteries", *Additive Manufacturing*. vol. 23 p.70–78, 2018.
  62. C.W. Foster, M.P. Down, Y. Zhang, X. Ji, S.J. Rowley-Neale, G.C. Smith, P.J. Kelly, C.E. Banks, "3D Printed Graphene Based Energy Storage Devices", *Scientific Reports*. vol. 7, 2017.
  63. T.D. Brown, P.D. Dalton, D.W. Hutmacher, "Direct Writing By Way of Melt Electrospinning", *Advanced Materials*. vol. 23 p.5651–5657. 2011.
  64. G. Hochleitner, T. Jüngst, T.D. Brown, K. Hahn, C. Moseke, F. Jakob, P. Dalton, J. Groll "Additive manufacturing of scaffolds with sub-micron filaments via melt electrospinning writing", *Biofabrication*. vol. 7, 2015.
  65. G. Hochleitner, J.F. Hümmer, R. Luxenhofer, J. Groll, "High definition fibrous poly(2-ethyl-2-oxazoline) scaffolds through melt electrospinning writing", *Polymer*. vol. 55 p.5017–5023, 2014.
  66. G. Luo, K.S. Teh, X. Zang, D. Wu, Z. Wen, L. Lin, "High aspect-ratio 3D microstructures via near-field electrospinning for energy storage applications", IEEE 29th International Conference on Micro Electro Mechanical Systems (MEMS). 2016.
  67. C. Kim, B.T.N. Ngoc, K.S. Yang, M. Kojima, Y.A. Kim, Y. J. Kim, M. Endo, S. C. Yang "Self-Sustained Thin Webs Consisting of Porous Carbon Nanofibers for Supercapacitors via the Electrospinning of Polyacrylonitrile Solutions Containing Zinc Chloride", *Advanced Materials*. vol. 19, p.2341–2346, 2007.
  68. A. Azhari, E. Marzbanrad, D. Yilman, E. Toyserkani, M.A. Pope, "Binder-jet powder-

- bed additive manufacturing (3D printing) of thick graphene-based electrodes”, *Carbon*. vol. 119, p.257–266, 2017.
69. N. Shamsaei, A. Yadollahi, L. Bian, S.M. Thompson, “An overview of Direct Laser Deposition for additive manufacturing; Part II: Mechanical behavior, process parameter optimization and control”, *Additive Manufacturing*. vol. 8, p.12–35, 2015.
  70. C. Zhao, C. Wang, R. Gorkin, S. Beirne, K. Shu, G.G. Wallace, “Three dimensional (3D) printed electrodes for interdigitated supercapacitors”, *Electrochemistry Communications*. vol.41, p.20–23, 2014.
  71. X. Lu, T. Zhao, X. Ji, J. Hu, T. Li, X. Lin, W. Huang, “3D printing well organized porous iron-nickel/polyaniline nanocages multiscale supercapacitor”, *Journal of Alloys and Compounds*. vol. 760, p.78–83, 2018.
  72. J. Zhang, F. Dumur, P. Xiao, B. Graff, D. Bardelang, D. Gigmes, J. P. Fouassier, J. Lalevee, “Structure Design of Naphthalimide Derivatives: Toward Versatile Photoinitiators for Near-UV/Visible LEDs, 3D Printing, and Water-Soluble Photoinitiating Systems”, *Macromolecules*. vol. 48, p.2054–2063, 2015.
  73. B. Steyrer, P. Neubauer, R. Liska, J. Stampfl. “Visible Light Photoinitiator for 3D-Printing of Tough Methacrylate Resins”. *Materials*, vol. 10, p.1445, 2017.
  74. M.A. Meyers, K.K. Chawla. “Mechanical Behavior of Materials”, 9781107394186, Cambridge University Press, 2008.
  75. McNaught; Wilkinson, A.D., eds. (February 24, 2014). "Oligomer molecule". *Compendium of Chemical Terminology (the "Gold Book")* (2 ed.). Blackwell Scientific.
  76. R. Tajau, M.I. Ibrahim, N.M. Yunus, M.H. Mahmood, M.Z. Salleh, N.G.N. Salleh, “Development of palm oil-based UV-curable epoxy acrylate and urethane acrylate resins for wood coating application”, *AIP Conference Proceedings*. vol. 1584, 164–169, 2015.
  77. C.V.D. Anibal, M. Odena, I. Ruisánchez, M.P. Callao, “Determining the adulteration of spices with Sudan I-II-III-IV dyes by UV–visible spectroscopy and multivariate classification techniques”, *Talanta*. vol. 79, p.887–892, 2009.
  78. D.W. van Krevelen, Klaas te Nijenhuis, “Properties of Polymers: Their Correlation with Chemical Structure”, 784p, 2009.
  79. X. Zheng, J. Deotte, M.P. Alonso, G.R. Farquar, T.H. Weisgraber, S. Gemberling, et al., “Design and optimization of a light-emitting diode projection micro-

- stereolithography three-dimensional manufacturing system", vol. 84, p.019902, 2013.
80. Applied Mechanics and Materials Vols. 465-466 (2014) pp 911-915 © (2014) Trans Tech Publications, Switzerland doi:10.4028/www.scientific.net/AMM.465-466.911
  81. Nuclear Instruments and Methods in Physics Research Section B: Beam Interactions with Materials and Atoms, Volume 151, Issues 1–4, 2 May 1999, Pages 22-28
  82. Progress in Organic Coatings, Volume 58, Issues 2–3, 1 February 2007, Pages 146-157
  83. S. I. White, R. M. Mutiso, P. M. Vora, D. Jahnke, S. Hsu, J. M. Kikkawa, J. Li, J. E. Fischer, and K. I. Winey, "Electrical Percolation Behavior in Silver Nanowire–Polystyrene Composites: Simulation and Experiment," *Adv. Funct. Mater.*, vol. 20, p. 2709–2716, 2010.
  84. W. Xu, Q. Xu, Q. Huang, R. Tan, W. Shen, W. Song, "Electrically conductive silver nanowires-filled methylcellulose composite transparent films with high mechanical properties," *Mater. Lett.*, vol. 152, pp. 173-176, 2015.
  85. T. Aktar, W. S. Kim, "Reversibly Stretchable Transparent Conductive Coatings of Spray-deposited Silver Nanowires" *ACS Applied Materials & Interfaces*, vol. 4, p.1855-1859, 2012.
  86. K. Na, S. Shin, H. Lee, D. Shin, J. Baek, H. Kwak, M. Park, J. Shin, J. Hyun, "Effect of solution viscosity on retardation of cell sedimentation in DLP 3D printing of gelatin methacrylate/silk fibroin bioink". *J. Ind. Eng. Chem.* vol. 61, p.340–347, 2018.
  87. C. W. Chang, Y. C. Liao, "Accelerated Sedimentation Velocity Assessment for Nanowires Stabilized in a Non-Newtonian Fluid". *Langmuir*. vol. 32, p.13620–13626, 2016.
  88. H. Gong, M. Beauchamp, S. Perry, A. T. Woolley, G. P. Nordin, "Optical approach to resin formulation for 3D printed microfluidics". *RSC Adv.* vol. 5, p.106621–106632, 2015.
  89. S. Zissi, A. Bertsch, J. Y. Jezequel, S. Corbel, D. J. Lougnot, J. C. Andre, "Stereolithography and microtechniques". *Microsyst. Technol.* vol. 2, p. 97–102, 1996.
  90. C. Sun, N. Fang, D. M. Wu, X. Zhang, "Projection microstereo lithography using digital micro-mirror dynamic mask". *Sens. Actuators, A* vol. 121, p.113–120, 2005.
  91. Z. Weng, Y. Zhou, W. Lin, T. Senthil, L. Wu, "Structure property relationship of nano enhanced stereolithography resin for desktop SLA 3D printer". *Composites, Part A*,

- vol. 88, p.234–242, 2016.
92. W. T. Chang, H. J. Hsu, C. P. Jiang, S. Y. Lee, Y. M. Lin, “Effects of titanium dioxide and tartrazine lake on Z-axis resolution and physical properties of resins printed by visible-light 3D printers”. *Rapid Prototyping J.* vol. 24, p.160–165, 2018.
  93. Y. Yang, Z. Chen, X. Song, B. Zhu, T. Hsiai, P. I. Wu, R. Xiong, J. Shi, Y. Chen, Q. Zhou, K. K. Shung. “Three Dimensional Printing of High Dielectric Capacitor Using Projection Based Stereolithography Method”. *Nano Energy*, vol. 22, p.414–421, 2016.
  94. F. P. Jacobs, D. T. Reid, “Rapid prototyping and manufacturing: fundamentals of stereolithography”; Society of Manufacturing Engineer: Dearborn, MI, 1992.
  95. Y. Han, C.C.J. Yeo, D. Chen, F. Wang, Y. Chong, X. Li, X. Jiao, F. K. Wang, “Nanowire enhanced dimensional accuracy in acrylate resin-based 3D printing”. *New J. Chem.* vol. 41, p.8407–8412, 2017.
  96. R. H. Halvorson, R. L. Erickson, C. L. Davidson, “The effect of filler and silane content on conversion of resin-based composite”. *Dent. Mater.* vol. 19, p.327–333, 2003.
  97. J. S. Park, T. Kim, W. S. Kim, “Conductive Cellulose Composites with Low Percolation Threshold for 3D Printed Electronics”. *Sci. Rep.* vol. 7, p.3246, 2017.
  98. T. Kim, L. Trangkanukulkij, W. S. Kim. “Nozzle Shape Guided Filler Orientation in 3D Printed Photo-curable Nanocomposites”. *Sci. Rep.* vol. 8, p.3805, 2018.
  99. M. Kaur, T. Yun, S. Han, E. L. Thomas, W. S. Kim, “3D Printed Stretch-dominated Micro-trusses”. *Mater. Des.* vol. 134, p.272–280, 2017.
  100. P. Fratzl, R. Weinkamer, “Nature’s hierarchical materials”. *Prog. Mater. Sci.* vol. 52, p.1263–1334, 2007.
  101. L. R. Meza, A. J. Zelhofer, N. Clarke, A. J. Mateos, D. M. Kochmann, J. R. Greer, “Resilient 3D hierarchical architected metamaterials”. *Proc. Natl. Acad. Sci. U. S. A.* vol. 112, p.11502–11507, 2015.
  102. S. R. Johnston, M. Reed, H. Wang, D.W. Rosen, “Analysis of Mesostructure Unit Cells Comprised of Octet-truss Structures”. *Proceedings of the Solid Freeform Fabrication Symposium, Aug 14–16*, p.421–432, 2006.
  103. L. Dong, H. Wadley, “Shear response of carbon fiber composite octet-truss lattice structures”. *Composites, Part A.* vol. 81, p.182–192, 2016.
  104. J. M. Gere, B. J. Goodno, “Mechanics of Materials”, 8th ed.; Cengage Learning: Stamford, pp 354–420, 2012.

105. P. Tian, C. Chen, J. Hu, J. Qi, Qi. Wang, J.C.M. Chen, J. Cavanaugh, Y. Peng, M.M.C. Cheng, "A novel fabrication method of carbon electrodes using 3D printing and chemical modification process" *Biomed. Microdevices*. vol. 20 p.4–9, 2018.
106. J. S. Choi, J. Seo, S. B. Khan, E. S. Jang, H. Han, "Effect of Acrylic Acid on the Physical Properties of UV-Cured Poly(Urethane Acrylate-Co-Acrylic Acid) Films for Metal Coating". *Prog. Org. Coat.* vol. 71, p.110–116, 2011.
107. D. P. Langley, M. Lagrange, G. Giusti, C. Jiménez, Y. Bréchet, N. D. Nguyen, D. Bellet, "Metallic Nanowire Networks: Effects of Thermal Annealing on Electrical Resistance" *Nanoscale*. vol. 6, p.13535–13543, 2014.
108. J. Plateau, Translated Annual Reports of the Smithsonian Institution 1873, 1863.
109. L. Rayleigh, Proc. London Math. Soc. 1878, s1–10, 4–13.
110. Y. Dong, B. Jia, F. Fu, H. Zhang, L. Zhang, J. Zhou, "Fabrication of Hollow Materials by Fast Pyrolysis of Cellulose Composite Fibers with Heterogeneous Structures". *Angew. Chem Int.Ed.* vol. 55, p.13504–13508, 2016.
111. Y. Liu, J. Zhang, H. Gao, Y. Wang, Q. Liu, S. Huang, C.F. Guo, Z. Ren, "Capillary-Force-Induced Cold Welding in Silver-Nanowire-Based Flexible Transparent Electrodes." *Nano Lett.* vol. 17, p.1090–1096, 2017.
112. G. Wee, W. F. Mak, N. Phonthammachai, A. Kiebele, M. V. Reddy, B.V.R. Chowdari, G. Gruner, M. Srinivasan, S. G. Mhaisalkar, "Particle Size Effect of Silver Nanoparticles Decorated Single Walled Carbon Nanotube Electrode for Supercapacitors." *J. Electrochem. Soc.*, vol. 157, p.A179–A184, 2010.
113. D. S. Patil, S. A. Pawar, R. S. Devan, M. G. Gang, Y. R. Ma, J. H. Kim, P. S. Patil, "Electrochemical supercapacitor electrode material based on polyacrylic acid/polypyrrole/silver composite". *Electrochim. Acta*, vol. 105, p.569–577, 2013.
114. G. Yu, L. Hu, N. Liu, H. Wang, M. Vosgueritchian, Y. Yang, Y. Cui, Z. Bao, "Enhancing the Supercapacitor Performance of Graphene/MnO<sub>2</sub> Nanostructured Electrodes by Conductive Wrapping". *Nano Lett.* vol. 11, p.4438–4442, 2011.
115. Y. Zhu, S. Murali, M. D. Stoller, K. J. Ganesh, W. Cai, P. J. Ferreira, A. Pirkle, R. M. Wallace, K. A. Cychoz, M. Thommes, D. Su, E. A. Stach, R. S. Ruoff, "Carbon-Based Supercapacitors Produced by Activation of Graphene". *Science*, vol. 332, p.1537–1541, 2011.
116. F. Béguin, V. Presser, A. Balducci, E. Frackowiak, "Carbons, Electrolytes for Advanced Supercapacitors". *Adv. Mater.* vol. 26, p.2219–2251, 2014.
117. B. G. Choi, M. H. Yang, W. H. Hong, J. W. Choi, Y. S. Huh, Y. "3D macroporous

graphene frameworks for supercapacitors with high energy and power densities". *ACS Nano*, vol. 6, p.4020–4028, 2012.

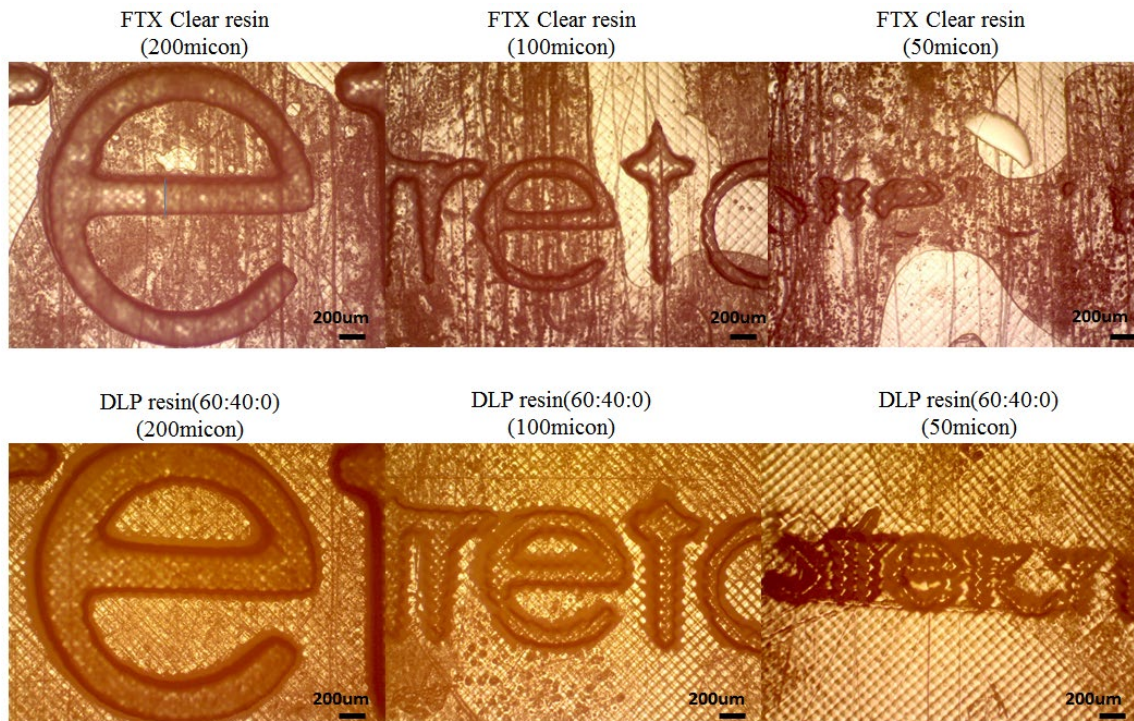
## Appendix A.

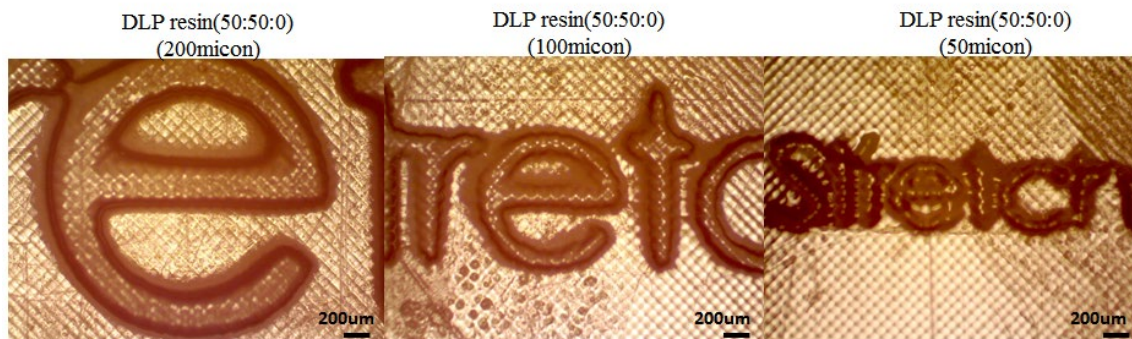
### Resin cartridge of DLP printer



## Appendix B.

### Resolution test





Optical microscope image of DLP printed samples to study lowest printable width (Letter: stretch).

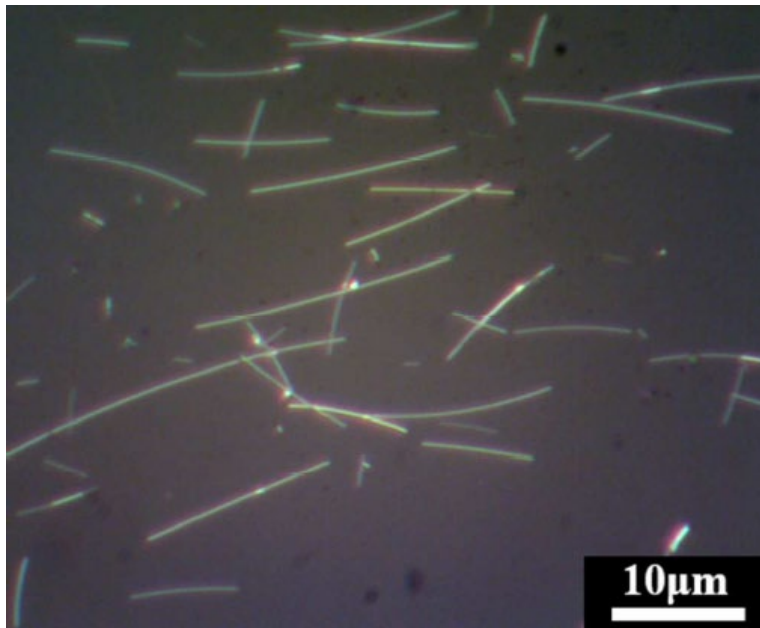
## Appendix C.

### Silver nanowire synthesis



Photograph of AgNW synthesis





Optical microscope image of AgNWs  
(as synthesized) in isopropyl alcohol solvent

## Appendix D.

### Printed samples on the platform

